

Simulating Impacts of Real-World Wind Farms on Land Surface Temperature Using the WRF Model: Validation with Observations

GENG XIA,^a MATTHEW C. CERVARICH,^b SOMNATH BAIDYA ROY,^c LIMING ZHOU,^a
JUSTIN R. MINDER,^a PEDRO A. JIMENEZ,^d AND JEFFREY M. FREEDMAN^e

^a *Department of Atmospheric and Environmental Sciences, University at Albany,
State University of New York, Albany, New York*

^b *Department of Atmospheric Sciences, University of Illinois at Urbana–Champaign, Urbana, Illinois*

^c *Centre for Atmospheric Sciences, Indian Institute of Technology Delhi, Hauz Khas, New Delhi, India*

^d *Research Applications Laboratory, NCAR, Boulder, Colorado*

^e *Atmospheric Sciences Research Center, University at Albany, State University of New York, Albany, New York*

(Manuscript received 19 October 2016, in final form 10 September 2017)

ABSTRACT

This study simulates the impacts of real-world wind farms on land surface temperature (LST) using the Weather Research and Forecasting (WRF) Model driven by realistic initial and boundary conditions. The simulated wind farm impacts are compared with the observations from the Moderate Resolution Imaging Spectroradiometer (MODIS) and the first Wind Forecast Improvement Project (WFIP) field campaign. Simulations are performed over west-central Texas for the month of July throughout 7 years (2003–04 and 2010–14). Two groups of experiments are conducted: 1) direct validations of the simulated LST changes between the preturbine period (2003–04) and postturbine period (2010–14) validated against the MODIS observations; and 2) a model sensitivity test of LST to the wind turbine parameterization by examining LST differences with and without the wind turbines for the postturbine period. Overall, the WRF Model is moderately successful at reproducing the observed spatiotemporal variations of the background LST but has difficulties in reproducing such variations for the turbine-induced LST change signals at pixel levels. However, the model is still able to reproduce coherent and consistent responses of the observed LST changes at regional scales. The simulated wind farm-induced LST warming signals agree well with the satellite observations in terms of their spatial coupling with the wind farm layout. Moreover, the simulated areal mean warming signal (0.20°–0.26°C) is about a tenth of a degree smaller than that from MODIS (0.33°C). However, these results suggest that the current wind turbine parameterization tends to induce a cooling effect behind the wind farm region at nighttime, which has not been confirmed by previous field campaigns and satellite observations.

1. Introduction

Widely acknowledged as a key resource to reduce the world's dependence on fossil fuels and decrease carbon emissions, wind energy has experienced a remarkable growth in recent years [(American Wind Energy Association) AWEA 2015] and the number of wind turbines is expected to increase nearly fivefold by 2030 (U.S. DOE 2015). The richest resources of onshore wind power in the United States are over the Great Plains,

home to most of the nation's wheat and corn production. While the collocation of wind farms with intensively managed agricultural production is possible, it brings up the concern of whether the widespread deployment of wind farms may affect agricultural activity through their interactions with the planetary boundary layer (PBL) (Rajewski et al. 2013, 2014; Armstrong et al. 2014; Tang et al. 2017; Xia and Zhou 2017). Hence, understanding wind farms and PBL–microclimate interactions will be critical for the sustainable growth of wind energy in the United States.

Using in situ observations, Baidya Roy and Traiteur (2010) first found that large wind farms tend to induce surface warming when the boundary layer is stably stratified at nighttime, but cause surface cooling at daytime. Similar nighttime impacts were also confirmed by Smith

Supplemental information related to this paper is available at the Journals Online website: <https://doi.org/10.1175/MWR-D-16-0401.s1>.

Corresponding author: Geng Xia, gxia@albany.edu

et al. (2013) and Rajewski et al. (2013, 2014, 2016) from their field campaigns but no obvious daytime impacts were found. Zhou et al. (2012, 2013a,b), using Moderate Resolution Imaging Spectroradiometer (MODIS) data (Wan 2008), observed an area mean land surface temperature (LST) warming signal up to 0.7°C that is spatially well coupled with several wind farms in west-central Texas during summer (June–August) nighttime, but found no significant impacts at daytime. Following the approaches in Zhou et al. (2012), Harris et al. (2014) and Slawsky et al. (2015) identified similar LST changes over wind farms in Iowa and Illinois; Chang et al. (2016) found similar nighttime LST impacts from a large-scale wind farms in Guazhou, China. Using sonic detection and ranging (sodar) observations from the first Wind Forecast Improvement Project (WFIP; Wilczak et al. 2015) and MODIS data, Xia et al. (2016) showed that variations in the ratio of turbulence kinetic energy (TKE) induced by wind turbines relative to the background TKE help to explain not only the day–night contrast of the wind farm impact on LST, but also most of the seasonal variability in the turbine-induced nighttime LST changes.

Because of the limited availability of field data, numerical modeling continues to be a primary tool to study the effects of wind farms on meteorology at a wide range of spatial and temporal scales. Wind turbine parameterization has been employed in three distinct modeling contexts: 1) large-eddy simulation (LES) models (Cal et al. 2010; Calaf et al. 2010, 2011; Lu and Porté-Agel 2011; Porté-Agel et al. 2011; Wu and Porté-Agel 2011, 2013; Churchfield et al. 2012; Mirocha et al. 2014; Creech et al. 2015), 2) mesoscale models (Baidya Roy et al. 2004; Baidya Roy 2011; Fitch et al. 2012, 2013a; Cervarich et al. 2013), and 3) global climate models (Keith et al. 2004; Kirk-Davidoff and Keith 2008; Barrie and Kirk-Davidoff 2010; Wang and Prinn 2010, 2011). High-resolution LES is computationally too expensive to simulate large operational wind farms (more than 1000 wind turbines), while coarse-resolution climate models may fail to accurately recreate turbulence in turbine wakes (Fitch et al. 2013b; Fitch 2015). Hence, mesoscale models provide an optimal way of investigating wind farm impacts at regional scales.

Baidya Roy et al. [2004; see also Baidya Roy (2011)] first used a mesoscale approach to simulate hypothetical wind farms in Oklahoma and developed a parameterization scheme that approximated the effect of a wind turbine as a sink of momentum or mean state kinetic energy and source of TKE. Using a similar approach, Fitch et al. (2012) developed a more sophisticated wind turbine parameterization for the Weather Research and Forecasting (WRF) Model (Skamarock and Klemp 2008) and produced results comparable with those

simulated with LES and observed in wind tunnels. Fitch et al. (2013a) examined the influences of wind farms throughout a diurnal cycle in an idealized simulation and found a near-surface warming of 0.5 K and cooling up to -0.3 K downwind (10–20 km) of the wind farms. Typically, the warming occurred during the night and early mornings when the environment was stably stratified whereas the small cooling signal was seen during the morning transition.

Although previous modeling results have shown some skill in reproducing potential local and regional effects of wind farms on weather and climate, direct and comprehensive validation of model output against observations is still very limited. This is because most of the studies have used hypothetical wind farms often with idealized initial and boundary conditions. Cervarich et al. (2013) first tried to evaluate the ability of mesoscale models in simulating seasonal-scale changes in LST over real-world wind farms in west-central Texas for the summer of 2010 under realistic boundary conditions. They confirmed the major observational findings of Zhou et al. (2012), but their simulated LST impacts were too weak and did not show strong spatial correspondence to the layout of wind turbines shown in MODIS observations. In addition, there were only 4 levels in the lowest 300 m in their simulations, which is probably not adequate to resolve vertical turbulent transport within the wind farms [the typical turbine rotor plane for 1.5 MW wind turbine spans 40–120 m above ground level (AGL)]. Furthermore, their monthlong simulation was initialized only once and thus surface conditions may have drifted from the forcing reanalysis during the course of long integration (Lo et al. 2008). At the same time, running a long-term mesoscale simulation in sequence of short runs with multiple reinitialization has been increasingly used (Pan et al. 1999; Qian et al. 2003; Lo et al. 2008; Conil and Hall 2006; Jiménez et al. 2010, 2015) and was recently adopted in wind farm modeling. For instance, Jiménez et al. (2015) compared the WRF-simulated power deficits associated with wind turbine wakes with observations created from a supervisory and data acquisition system. They prescribed a total of 36 vertical levels, 5 of which were within the lowest 200 m of the atmosphere, and conducted simulations with a 2-day reinitialization for a 3-yr period. Their results indicated that the WRF Model can qualitatively reproduce the turbine–flow interactions under different atmospheric conditions but the model tended to underestimate the power deficit. This reinitialization method has the advantage of frequently updating realistic surface conditions. However, it is still unclear which initialization method (continuous vs reinitialized) is more suitable for wind farm modeling as

both have limitations. For the continuous simulation, the surface condition was initialized only once in the beginning of the simulation and thus may have drifted from the forcing reanalysis if the simulation period is too long. However, the continuous simulation can allow for persistent and physically consistent wind farm effects, since soil properties are not constantly reinitialized. The reinitialized simulation has the advantage of frequent updated surface conditions but the uncertainties caused by abrupt surface changes (e.g., soil moisture) between short runs may produce large uncertainties because of a lack of adequate spinup (Pan et al. 1999; Qian et al. 2003). Such uncertainties will be smaller because of consistent surface conditions in the continuous runs.

Here we assess the WRF Model's ability in simulating real-world wind farm effects on LST to address one important question: How accurate is the WRF's wind turbine parameterization in reproducing the LST changes observed by MODIS? Both the continuous and 3-day reinitialized simulations are performed. The simulated LST responses to operational wind farms are validated against the MODIS observations and the simulated wind conditions are validated against the WFIP measurements. The region of interest is a collocation of several large wind farms located in west-central Texas. This area is particularly rich in wind resources and has been explored in previous studies (Zhou et al. 2012, 2013a,b; Xia et al. 2016). The remainder of the paper is divided into four sections. The data and methods employed are described in section 2. The model's ability to reproduce the observed LST signal is analyzed in detail in section 3. Uncertainties associated with the model simulation, data, and methodology are discussed in section 4, followed by the conclusions in section 5.

2. Observations, experiment design, and methodology

a. Study region and period

Our study region (Fig. 1) is in west-central Texas covering a group of large wind farms consisting of 2358 wind turbines. This region has previously been examined using the observational data from MODIS (Zhou et al. 2012, 2013a,b) and the first WFIP field campaign (Xia et al. 2016). These studies show that the strongest wind farm impact signal on LST and its best spatial coupling with the wind turbines occur during the summer months. The geographic location and operational date for each turbine are obtained from the Federal Aviation Administration Obstruction Evaluation/Airport Airspace Analysis dataset (https://www.fws.gov/southwest/es/Energy_Wind_FAA.html). Among the

2358 wind turbines, 2122 (~90%) were built during the period 2005–09. Following Xia et al. (2016), our study covers the period 2003–14 and we choose the preturbine period from 2003 to 2004 and the postturbine period from 2010 to 2014 for the comparative analyses. Because of the limitation of computational resources for high-resolution WRF simulations, we focus only on the month of July for both periods.

b. Data and experiment design

1) MODIS LST DATA

Version 6 MODIS 8-day average 1-km LST products (Wan 2008) are used in this study. MODIS is a key scientific satellite instrument launched by NASA on board the *Terra* and *Aqua* platforms. The MODIS LST images consist of four acquisition times: ~1030 and ~1330 local solar time (LT) during the day and ~2230 and ~0130 LT at night. The retrieved MODIS LST data are known to be most accurate during cloud-free conditions (Wan 2002, 2008). For every MODIS 8-day average image, only the best quality clear-sky pixels are chosen to represent LST measurements within each 8-day period based on MODIS quality assurance information following the methodology of Zhou et al. (2013a). The MODIS data for the period 2003–14 are processed using the methodology of Xia et al. (2016) to produce the monthly mean LST and LST anomalies. Readers are encouraged to refer to this paper for full details.

2) SODAR DATA

Sodar data from the first WFIP field campaign (Wilczak et al. 2015; Freedman et al. 2014) are used to validate the simulated wind conditions. The first WFIP field campaign includes sodar observations from mid-July 2011 to September 2012 and so validation efforts focus on the simulated wind climate in July 2012. We computed the hourly wind speed and wind direction from the postprocessed sodar data from one WFIP station, Colorado City, Texas (the green dot in Fig. 1b), which is located 11 km away from the targeted wind farms. However, there are only 11 days of observations available in July 2012 because of a lightning strike that destroyed the site. Please refer to Xia et al. (2016) for more details about the first WFIP and the sodar data.

3) WRF MODEL AND EXPERIMENT DESIGN

The numerical model chosen for our simulations is the Advanced Research WRF (WRF-ARW, v3.6.1), which is a fully compressible and nonhydrostatic model. Its

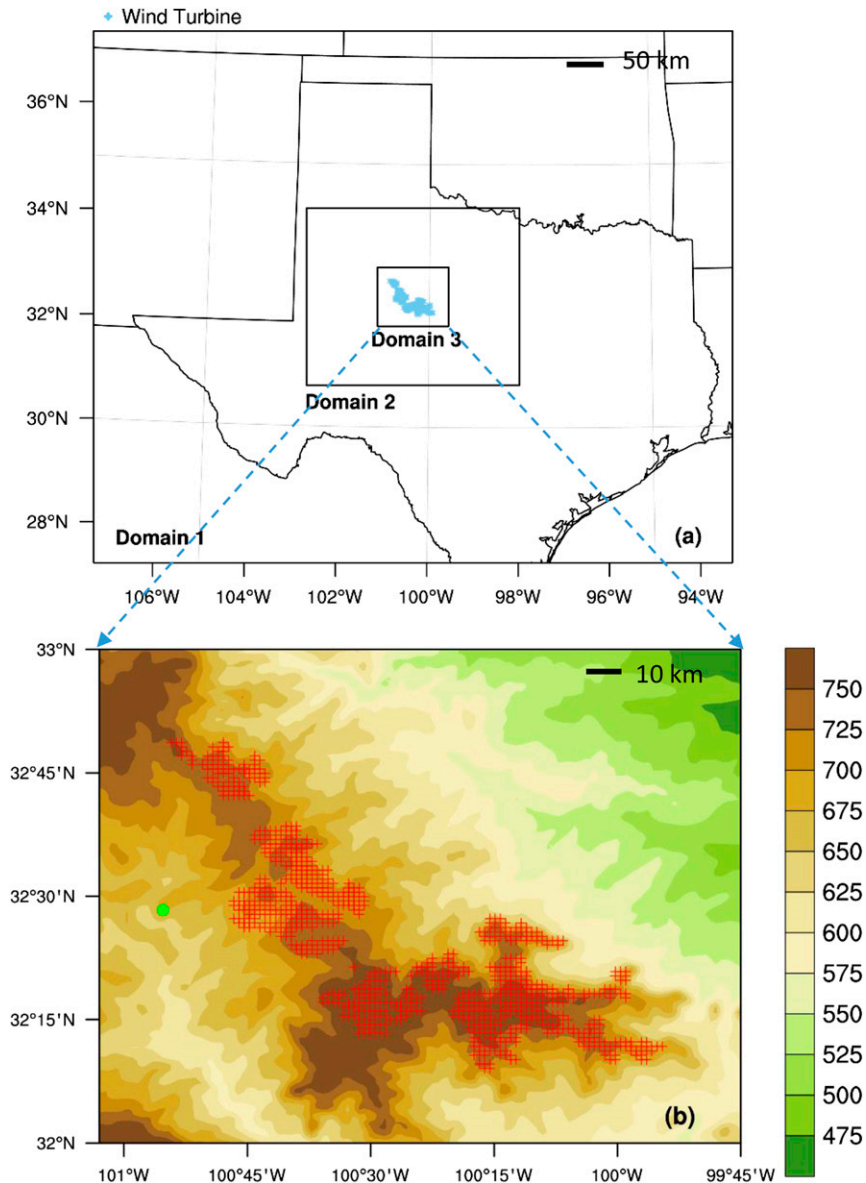


FIG. 1. The three simulation domains and elevation map (m): (a) the simulation region along with the three nested domains and (b) the elevation map of Domain 3. The blue asterisks in (a) and the red crosses in (b) mark the locations of individual wind turbines. The green dot in (b) indicates the location of the WFIP station, Colorado City, TX, where the sodar measurements were taken.

vertical coordinate is a terrain-following hydrostatic pressure coordinate. The grid staggering is the Arakawa C grid. The model uses the Runge–Kutta third-order time integration schemes, and fifth- and third-order advection schemes in the horizontal and vertical, respectively. It uses a time-split small step for the acoustic and gravity wave modes. The model configuration (physics parameterization) is summarized in Table 1. Both the boundary and initial conditions are from the North American

Regional Reanalysis (NARR; 32-km resolution). Note that soil moisture as well as soil temperature profiles (four layers) are also obtained from NARR. The topography, soil characteristics, and USGS-based land cover data are obtained from the WRF standard datasets. In addition, horizontal advection of TKE by the model dynamics is employed. At higher resolution (<1 km), it becomes essential to advect TKE downstream before being dissipated (Fitch et al. 2012).

TABLE 1. Summary of WRF Model configuration.

Shortwave	Dudhia scheme (Dudhia 1989)
Longwave	Rapid Radiative Transfer Model (Mlawer et al. 1997)
Microphysics	WRF single-moment 3-class (Hong et al 2004)
Cumulus	Kain–Fritsch scheme (Kain 2004)
Boundary layer	MYNN 1.5-order scheme (Mellor and Yamada 1982; Nakanishi and Niino 2009)
Land surface	Noah-MP (Yang et al. 2011; Niu et al. 2011)

The simulations are performed with three nested domains centered at 32.50°N latitude, 100.375°W longitude (Fig. 1a) in the study region. Domain 1, the coarsest domain, consists of 55×46 grid points with horizontal grid spacing of 25 km. The two nested domains, domain 2 and domain 3, have horizontal grid spacing of 5 km (91×76) and 1 km (151×126), respectively. Corresponding geographic and topographic datasets from the U.S. Geological Survey with similar resolution (20 km, 4 m, and 1 km) are chosen to match each grid spacing. The boundary of the innermost domain is determined so that the turbines are located at least 25 km from the domain edge to ensure that numerical boundary feedback issues do not create artificial signals. The three domains communicate via an interactive two-way nesting scheme. Note that cumulus convection is treated explicitly in domain 3 but is parameterized in the other two domains. The Mellor–Yamada–Nakanishi–Niino PBL scheme (MYNN; Nakanishi and Niino 2009) is used because it is the only PBL scheme that is compatible with the current wind turbine parameterization. A stretched vertical grid consisting of 39 levels is employed with finer resolution at lower levels and coarser resolution at higher levels. The grid contains 10 levels within the lowest 200 m to represent vertical transport in the wind turbine layer. The soil model is 2 m deep with 4 levels stretched in the vertical with higher resolution near the surface and lower resolution at deeper levels.

The WRF wind turbine parameterization was developed by Fitch et al. (2012). The parameterization represents the effect of a wind turbine by imposing a momentum sink term and a TKE source term onto the model layer containing the wind turbine. In this study, we use the 1.5-MW Pennsylvania State University Generic turbine coefficients (Schmitz 2012). For uniformity, all wind turbines are assumed to have 80-m hub height, 80-m rotor diameter, 3 m s^{-1} cut-in speed, and 25 m s^{-1} cut-out speed. The cut-in and cut-out speeds represent the range at which the wind turbine operates. If multiple turbines

are located within a single grid cell, changes in kinetic energy and TKE are multiplied by the number of turbines within the cell and integrated over the cell. The turbine blades are assumed to be oriented perpendicular to the wind as this is how turbines operate.

Two groups of experiments are conducted for the month of July during the pre- and postturbine periods. The first group of experiments (EXP1) aims to directly compare the simulated LST changes with MODIS observations to assess the model's ability to simulate the real-world wind farm impacts on LST. In EXP1, the actual number of wind turbines is included in the simulations. Figure 2a shows the geographical location of wind turbines for the preturbine (204 turbines, red crosses) and postturbine (2358 turbines, black crosses) periods, respectively. Essentially, EXP1 is a test of model skills but has the disadvantage by introducing additional LST uncertainties because of the model's difficulty in reproducing the observed natural year-to-year variability. The second group of experiments (EXP2) aims to assess the sensitivity of LST to the wind turbine parameterization by examining the LST differences with and without the presence of wind turbines for the postturbine period. It is a controlled experiment where only the presence of wind turbines is altered. Thus, the results are easier to interpret physically. The trade-off is that there is no equivalent experiment in the observations to validate such results.

For each experiment, we use two types of initializations: 1) a 3-day reinitialization (referred to as 3Day), and 2) a continuous run (referred to as CON). Each 3Day simulation is initialized at 0000 UTC and run for 72 h, providing 15 short segments of 3Day runs, each with one day overlap, for 30 days of July. The first day of each 3Day run is discarded as spinup and the next two days are retained for further analysis. In each CON run, the simulation is initialized at 0000 UTC 1 July and run for 30 days until 0000 UTC 31 July.

Table 2 shows a summary of the experiments performed for this study. We ran the WRF Model for both the pre- and postturbine periods. For each period, we conduct monthly simulations with two different initialization methods and with or without the wind turbine parameterization. In total, there are 14 sets of monthly experiments (7 with the wind turbine parameterization and 7 without) conducted for both the 3Day and CON simulations.

c. Methodology

1) SEPARATING SIMULATION DAYS INTO CLOUDY AND CLOUD-FREE DAYS

Separating cloudy days and cloud-free days in our simulations is essential as the MODIS data provide the

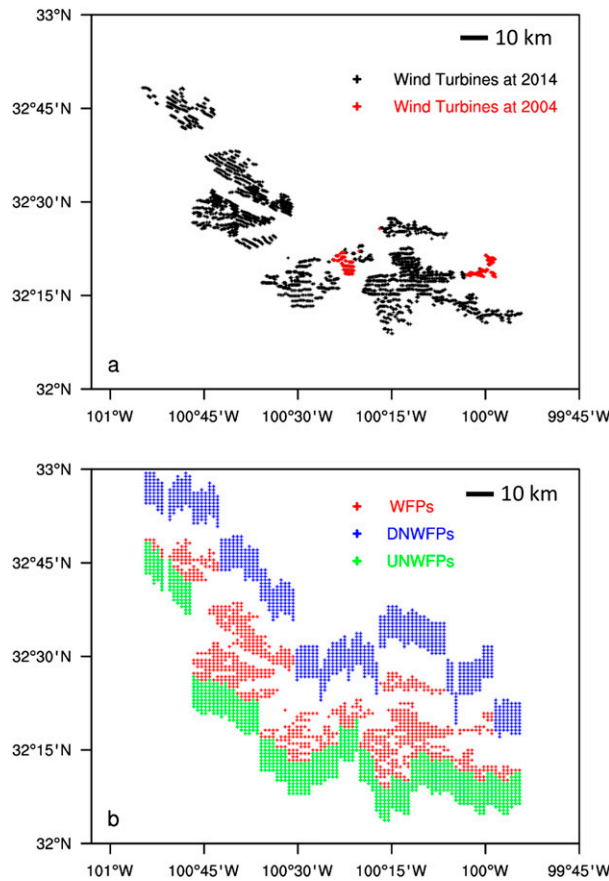


FIG. 2. The geographical location of actual wind turbines, WFPs, DNWFPs, and UNWFPs: (a) wind turbines in black used for the simulations conducted for the postturbine period whereas wind turbines in red for the preturbine period, (b) wind farm pixels (WFPs; 917 pixels in red), downwind nonwind farm pixels (DNWFPs; 940 pixels in blue), and upwind nonwind farm pixels (UNWFPs; 940 pixels in green). WFPs contain all 1-km grids with one or more wind turbines while DNWFPs (UNWFPs) represent pixels that are within 11–20 km (1–10 km) north (south) from WFPs.

best retrievals under cloud-free conditions. We calculate the cloud liquid water path (CLWP; kg m^{-2}) from the WRF default output and use it as an indicator to quantify the cloud cover (CC) in the domain. The equation is given below:

$$\text{CLWP} = \int_{z_{\text{bot}}}^{z_{\text{top}}} \rho_z q_c dz, \quad (1)$$

where z_{top} and z_{bot} are the vertical height at the bottom and top of the model domain, respectively; ρ_z is the air density (kg m^{-3}); q_c is the cloud water mixing ratio (kg kg^{-1}); and dz is the height between two neighboring vertical levels (m).

Since MODIS measurements are instantaneous values at ~ 2230 and ~ 0130 LT, we calculate CLWP at

TABLE 2. Summary of WRF experiments performed in this study.

Simulation period	Wind turbine parameterization
3-day reinitialization (3Day)	
Jul 2003–04	On
Jul 2003–04	Off
Jul 2010–14	On
Jul 2010–14	Off
Continuous simulation (CON)	
Jul 2003–04	On
Jul 2003–04	Off
Jul 2010–14	On
Jul 2010–14	Off

pixel level for every hour but only average those between 2200 and 0200 LT to create the CC map for each day. If a day has CC exceeding a threshold value of 0.02 kg m^{-2} for more than 15% of the entire wind farm region and its immediate vicinity (~ 5 km around the wind farm region), we consider that day as a cloudy day. The numbers of cloudy, cloud-free, and the total simulated days are listed in Table 3. There are considerably more cloud-free days than cloudy days, consistent with the study region's semiarid climate. Overall, 15% of all the simulated days (30 days) are considered as cloudy. In addition, there are no differences in the numbers of cloudy and clear-sky days selected for both the 3Day and CON runs, with 95% of the selected days being the same for both runs. To validate our simulations against the MODIS observations, only the model results from cloud-free days are used.

2) VALIDATING SIMULATED WIND CONDITIONS WITH SODAR OBSERVATIONS

Validating simulated wind conditions with sodar observations is essential as it enables us to properly characterize the resulting simulated wind farm impact on LST. The simulated wind over the grid cell closest to a WFIP field campaign site is used to compare with sodar observations. The elevation of the campaign site is 673 m whereas it is 675 m in the WRF Model. Since the turbine hub height and the turbine diameter are 80 m, we consider vertical ranges from 40 to 120 m AGL, corresponding to elevations between 710 and 790 m, to compute wind speed and wind direction statistics from both the WRF simulations and sodar. Note that the vertical resolution of sodar profiles is 10 m whereas it is 20 m for the lowest 200 m AGL in the WRF. In addition, only the results from the targeted nighttime hours (2200–0200 LT) for the 11 days are compared. Overall, 495 measurements from sodar are validated against 275 data points from the 3Day (or CON) simulations.

TABLE 3. The number of cloudy, cloud-free, and total days for all experiments simulated with the wind turbine parameterization off.

Expt	Cloudy days	Cloud-free days	Total days
Jul 2003	2	28	30
Jul 2004	9	21	30
Jul 2010	9	21	30
Jul 2011	0	30	30
Jul 2012	4	26	30
Jul 2013	2	28	30
Jul 2014	4	26	30
Ensemble	30	180	210

3) VALIDATING SIMULATED BACKGROUND LST WITH MODIS OBSERVATIONS

Validating simulated background LST with MODIS observations can assess whether the model can realistically simulate the spatiotemporal variability of LST over the study region. We compare the simulated spatial patterns of LST climatology and interannual variations of areal mean LST over the targeted region with the MODIS observations during July for 7 years (2003–04 and 2010–14).

4) VALIDATING SIMULATED TURBINE-INDUCED LST WITH MODIS OBSERVATIONS

Following Zhou et al. (2012, 2013a), if the operational wind turbines affect LST, the observed or simulated changes in LST should couple spatially with the layout of wind turbines. In EXP1, we estimate the wind farm impacts by examining the spatial patterns of LST changes between the pre- and postturbine periods. Since wind turbines are working during both periods (Fig. 2a), only the simulations with the wind turbine parameterization are used. In EXP2, the wind farm impact on LST is the difference between simulations with and without the wind turbine parameterization for the postturbine period.

Following Zhou et al. (2012, 2013a), we also quantify the wind farm impact on LST by comparing wind farm pixels (WFPs) with their nearby nonwind farm pixels (NNWFPs). The WFPs contain all the 1-km grids with one or more wind turbines. Since the wind is mostly southerly during the targeted nighttime hours (Zhou et al. 2013a), we consider two types of NNWFPs: 1) downwind nonwind farm pixels (DNWFPs; pixels within 11–20 km north from WFPs) and 2) upwind nonwind farm pixels (UNWFPs; pixels within 1–10 km south from WFPs). Note that DNWFPs are at least 10 km away from WFPs to minimize the downwind farm impacts. Figure 2b shows the geographic locations of WFPs (in red, 917 pixels in total), DNWFPs (in blue, 940 pixels in total), and

UNWFPs (in green, 940 pixels in total), respectively. The Student's t test is applied to quantify the statistical significance of the observed and simulated LST changes between the pre- and postturbine period for each group of pixels. A t value exceeding the 90% confident level (i.e., $p < 0.1$) is considered to be statistically significant.

The observed nighttime LST is the average of the two MODIS measurements at ~ 2230 and ~ 0130 LT whereas the simulated value is the 5-h average between 2200 and 0200 LT. The daytime comparison is omitted because previous satellite and field campaign studies suggest negligible wind farm impacts at daytime.

It is crucial to keep in mind that the wind farm impact on LST is small in magnitude and is a low-frequency signal, while the background LST varies dramatically on a daily and yearly basis and is a high-frequency signal. Therefore, we quantify the wind farm impact on LST via spatial and temporal averaging to enhance the low-frequency wind farm signal while minimizing high-frequency modeling uncertainties or smaller-scale natural variability (e.g., mesoscale storm systems) in individual runs. These points have been discussed extensively in previous papers (Zhou et al. 2012, 2013a,b; Harris et al. 2014; Slawsky et al. 2015; Xia et al. 2016).

3. Results and discussion

a. Wind statistics from cloud-free days in the WRF

Information on wind speed and direction across the rotor area is critical as it indicates whether the simulated wind turbines are operating. In addition, it enables us to properly characterize the resulting wind farm impact on LST. Figures 3a and 3b show the frequency distribution of wind speed and wind direction across the rotor area in the model simulations. Note that the frequencies are only calculated over the wind farm region during the targeted nighttime hours (2200–0100 LT) on all cloud-free days from the simulations without the wind turbine parameterization activated. Overall, only a negligible fraction of the simulated wind speed, 2%, is less than the cut-in (3 m s^{-1}) threshold across the rotor plane heights and most wind peaks between 6 and 9 m s^{-1} . These statistics indicate that the wind turbines over our study region are operating during most of the targeted nighttime hours in the WRF Model. As for wind direction, more than 95% of the time the wind is blowing from south or southeast, indicating that there could be potential downwind impacts on the northwestern and northern sides of the wind farm region.

b. Model's ability to simulate wind conditions

Figures 3c and 3d compare simulated wind conditions across the rotor plane heights (40–120 m AGL) from 2200 to 0200 LT for the 11 days in July 2012 with the

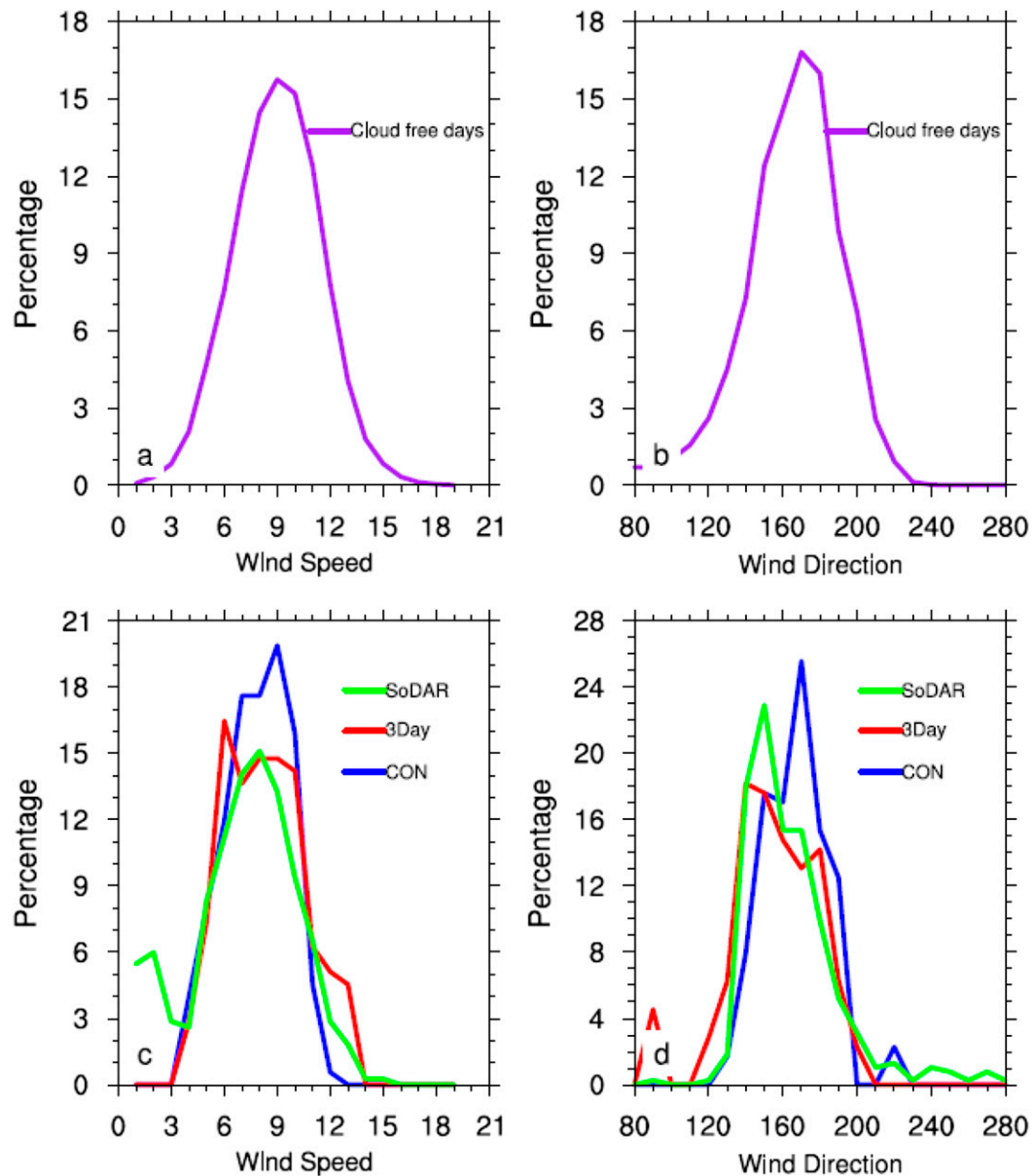


FIG. 3. Wind statistics across the rotor plane heights (40–120 m AGL) between 2200 and 0200 LT: (a) wind speed (m s^{-1}) distribution over the WFPs on all cloud-free days in WRF; (b) as in (a), but for wind direction; (c) wind speed (m s^{-1}) distribution for the 10 days in July 2012 from the 3Day, CON, and sodar; (d) as in (c), but for wind direction.

sodar observations. The average wind speed magnitude is 7.2 m s^{-1} from the sodar and 7.8 m s^{-1} from the WRF simulations. Moreover, $>85\%$ of wind speeds from the sodar and 95% from the simulations are within the range of $3\text{--}12 \text{ m s}^{-1}$. However, 15% of wind speeds measured by the sodar fall below the cut-in wind speed (3 m s^{-1}) but these low wind speeds are not reproduced by the simulations. This suggests that the WRF Model may overpredict the wind speed magnitude and thus

overestimate the simulated wind farm impacts in July 2012. As for wind direction, the averaged wind direction is 161° from the simulations and 160° from the sodar, respectively. About 85% of the total simulated wind directions and 84% of those from the sodar are between 120° and 200° . Therefore, the wind is mostly southerly or southeasterly over this region in July 2012. Overall, the WRF Model can qualitatively but not quantitatively reproduce the observed wind climate.

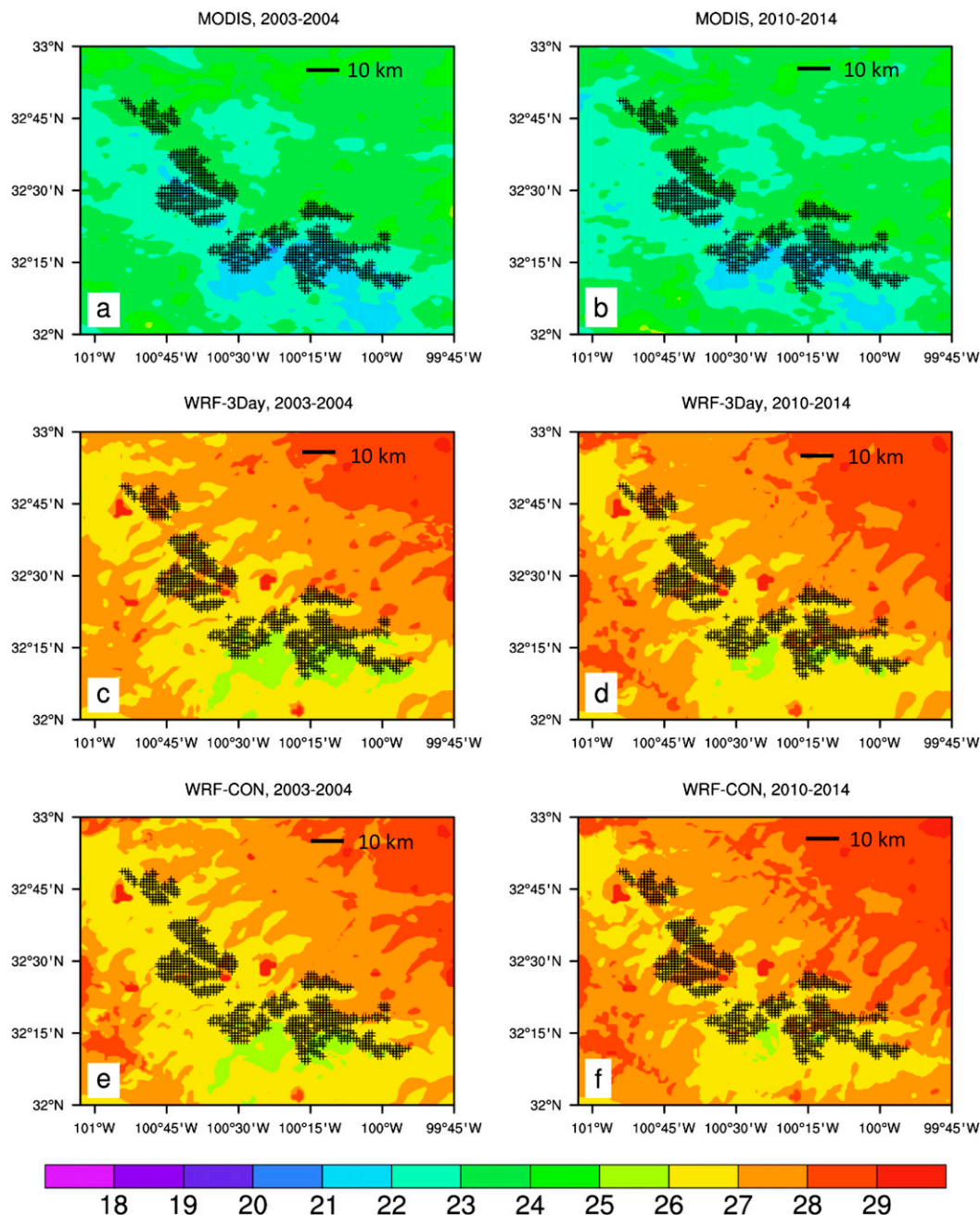


FIG. 4. Spatial pattern of July nighttime background LST ($^{\circ}\text{C}$) from MODIS and the WRF simulations (3Day and CON) for the pre- and postturbine periods: (a) MODIS, 2003–04; (b) MODIS, 2010–14; (c) 3Day, 2003–04; (d) 3Day, 2010–14; (e) CON, 2003–04; and (f) CON, 2010–14. The black dots indicate WFPs. The MODIS nighttime LST is averaged from the two nighttime measurements at ~ 2230 and ~ 0130 LT and the simulated nighttime LST is averaged from hourly model output between 2200 and 0200 LT.

c. Model's ability to simulate spatiotemporal variations of background LST

Figure 4 compares the spatial pattern of monthly averaged July nighttime LST climatology from MODIS and the WRF Model for the pre- and postturbine periods.

Both the WRF simulations and MODIS depict similar spatial patterns of LST with slightly warmer LST in the southwestern and northeastern part of the study domain and cooler LST over WFPs. The differences in LST values are mainly attributed to the variations in topography as shown in Fig. 1b, where the elevation is

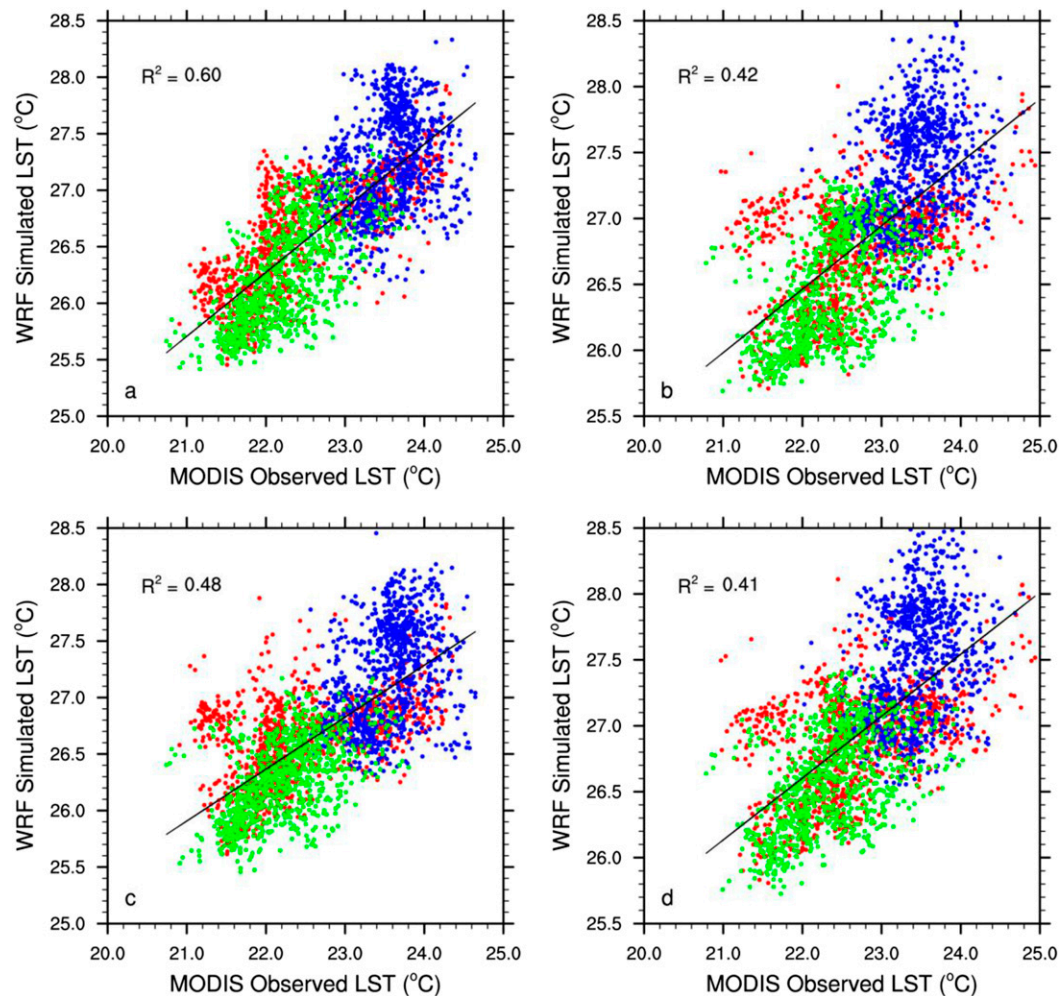


FIG. 5. Scatterplot of July nighttime background LST ($^{\circ}\text{C}$) between MODIS and the WRF simulations (3Day and CON): (a) MODIS and 3Day for the preturbine period, (b) MODIS and CON for the preturbine period, (c) MODIS and 3Day for the postturbine period, and (d) MODIS and CON for the postturbine period. The red, green, and blue dots represent WFPs (917 pixels), DNWFPs (940 pixels), and UNWFPs (940 pixels), respectively; R^2 stands for the coefficient of determination and is computed from all 2797 pixels. The black line represents the best fitting using linear regression.

relatively high over the center of the domain and low near the edge. The wind turbines are mostly located at the low temperature regions of the domain as they are generally built on topographic high ground. The simulated temperatures lack the finer spatial details of the observations because of the model's smoothed terrain. However, the simulated LST shows a positive bias ($\sim 3^{\circ}\text{C}$) as compared to MODIS observations. The uncertainty associated with this warm bias is discussed in more detail in section 3e. Nevertheless, this systematic bias is not expected to impact our simulated wind farm effects significantly as we are examining the simulated LST changes instead of the absolute values.

Figure 5 shows the scatterplots of the background LST climatology between MODIS and the WRF Model.

Figures 5a and 5b are the scatterplots between MODIS and 3Day runs, and between MODIS and CON runs for the preturbine period, respectively. Figures 5c and 5d are similar to Figs. 5a and 5b but for the postturbine period. In total, 2797 pixels are plotted in the figure. The red, green, and blue dots indicate WFPs, DNWFPs, and UNWFPs, respectively, while R^2 stands for the coefficient of determination, indicating how much spatial variability of the background LST from MODIS are captured by the WRF Model. The magnitude of the background LST over WFPs and UNWFPs are smaller than that over DNWFPs. The coefficient of determination (R^2) varies from 0.41 to 0.60, which, although not very high, is statistically significant ($p < 0.001$, $n = 2797$ where n is the sample size of pixel). Overall, the 3Day run has a higher

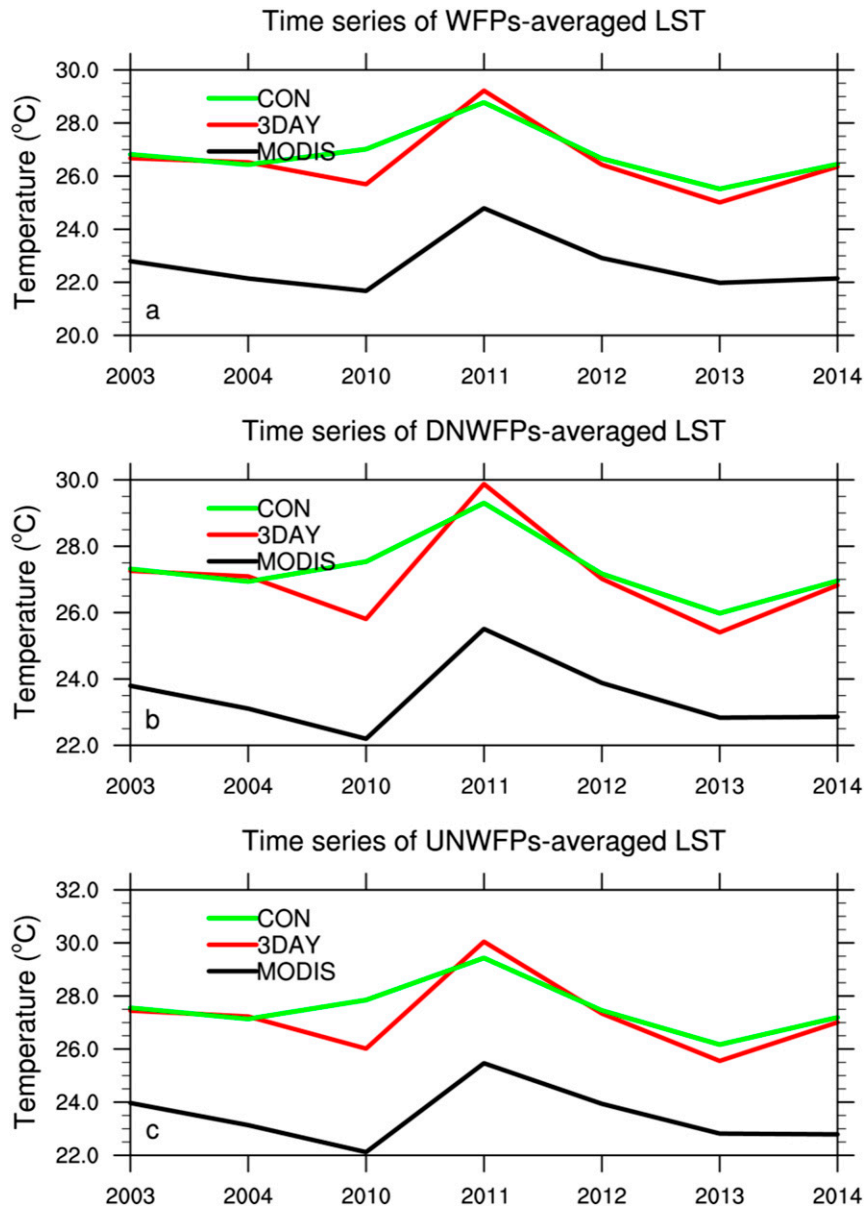


FIG. 6. Interannual variation of areal mean July nighttime LST ($^{\circ}\text{C}$) from MODIS (black), 3Day (red), and CON (green) simulations over WFPs, DNWFPs, and UNWFPs for 7 years (2003–04 and 2010–14): (a) WFPs-averaged LST, (b) DNWFPs-averaged LST, and (c) UNWFPs-averaged LST.

R^2 than the CON run because of reinitialization and there is a systematic nighttime LST warm bias in the WRF simulations compared to the MODIS observations.

To explore whether the interannual variations of the observed background LST can be simulated by the WRF Model, we calculate the areal mean LST values over WFPs, DNWFPs, and UNWFPs for each July month for both pre- and postturbine periods (2003–04 and 2010–14) from MODIS and the model (Fig. 6). The simulated LST captures the interannual variations of the observed LST

quite well, especially in the 3Day experiments. The simulated time series (3Day and CON) reproduce well the temperature anomaly associated with the 2011 severe drought in Texas. The correlation between the WRF simulations and MODIS is 0.92 ($p < 0.01$, $n = 7$) for the 3Day runs but 0.75 ($p < 0.01$, $n = 7$) for the CON runs, indicating the importance of having realistic surface condition in simulating local to regional climate. As with the previous plots, there is a clear warm bias in the model compared to the observations.

Overall, the spatial pattern and interannual variations of LST in MODIS are generally reproduced by the WRF simulations, indicating that the WRF Model, despite a systematic warm bias, simulates the spatial and interannual temporal LST variations over the study region moderately well, especially when the model is reinitialized to the NARR every 3 days.

d. Quantifying wind farm impacts on LST changes

1) SPATIAL PATTERNS OF LST CHANGES

Figure 7a shows the spatial patterns of MODIS nighttime LST changes in July between the post and preturbine periods. The LST warming signals are spatially well coupled with the wind farm layout, and most of the warming signals are in the range of 0.15°–0.55°C, with a maximum up to 1.20°C. Even though the wind direction is predominantly southeasterly and southerly, no noticeable distant (10 pixels, ~10 km) wind farm wake effect is observed. Overall, this result is consistent with previous studies (Zhou et al. 2012, 2013a; Xia et al. 2016). Note that there are patches of anomalous warming and cooling outside the wind farm region. Following Zhou et al. (2012, 2013a), a similar plot (see online supplemental Fig. S1) is created for the entire summer months and such signals either disappear or weaken, indicating that those patches are mainly due to high-frequency temporal LST variations, while the warming signals over the wind farm region remain robust and persistent.

Figures 7b and 7c show that the spatial patterns of the LST changes in both 3Day and CON are generally spatially coupled with the layout of wind turbines. For instance, 75% and 85% of WFPs in Figs. 7b and 7c indicate warming signals, smaller than that (~95%) in Fig. 7a. Note that the LST changes over WFPs containing a small number of operating turbines during the preturbine period (circled in green) do not show warming signals for either the 3Day runs or CON but they do show warming in the MODIS data. In general, the CON run has a stronger spatial coupling between the turbine layout and the LST warming signals while the 3Day run has a larger LST warming magnitude over WFPs. In addition, the model simulations produce a clear LST cooling signal downwind of the wind farm region, which is not clearly seen in the MODIS observations. Nevertheless, the current wind turbine parameterization successfully reproduces the observed spatial coupling between the warming signals and the wind turbine layout.

The statistical significance of the observed (Fig. 7a) and simulated (Figs. 7b,c) LST changes are examined and compared. For the MODIS observations, about

65% of the WFPs indicate statistically significant ($p < 0.01$, $n = 7$) warming signals whereas less than 20% of the DNWFPs and UNWFPs indicate significant LST changes (warming or cooling). In EXP1, only 50% of the WFPs from the 3Day simulation and 53% from the CON simulation indicate statistical significant warming signals. Furthermore, 60% and 55% of the DNWFPs from the 3Day and CON simulations indicate statistical significant cooling signals whereas less than 15% of the UNWFP suggest significant LST changes (warming or cooling). Therefore, the WRF produces a less significant warming over the WFPs but a much more significant cooling over the DNWFPs as compared to the MODIS observations.

Figure 8 shows the results from EXP2, which aims to assess the sensitivity of LST to the wind turbine parameterization by examining the LST differences with and without the presence of wind turbines for the post-turbine period. The LST warming pattern between 3Day (Fig. 8a) and CON (Fig. 8b) are very similar. Both the magnitude of the LST warming signal and its spatial coupling with the wind turbine layout are stronger in EXP2 than EXP1. More than 92% of WFPs show a warming signal. This increase in the percentage of the warming pixels is mostly contributed by WFPs during the preturbine period (circled in green). Furthermore, the cooling signal is mostly confined to the north of WFPs in EXP2 but more widely distributed in EXP1 possibly due to the residual signals of natural variations. However, there is a distinct downwind cooling effect in both EXP1 and EXP2 extending as far as 40 km away from the wind farms, which is less clear in the MODIS observations.

Figures 9a and 9b show the scatterplots of the LST changes between MODIS and 3Day runs, and between MODIS and CON runs from EXP1; Figs. 9c and 9d are the same but for EXP2. Evidently, R^2 for the LST changes is much smaller than that in Fig. 4, indicating that the WRF Model has difficulties in reproducing the spatial variations of observed LST changes at pixel levels, possibly due to simplified representation of surface heterogeneities (e.g., elevations, land use/soil classifications). However, the WRF Model is still able to reproduce the coherent responses of the observed LST changes for WFPs. For instance, more than 75% (90%) of WFPs in EXP1 (EXP2) indicate a warming signal. As in the observations, UNWFPs show noisy LST changes with both negative and positive values in both experiments. In contrast, more than 80% (95%) of DNWFPs in EXP1 (EXP2) indicate a cooling signal, while MODIS shows both negative and positive values. The consistent and coherent responses of the LST change signals between simulated and observed over WFPs, not

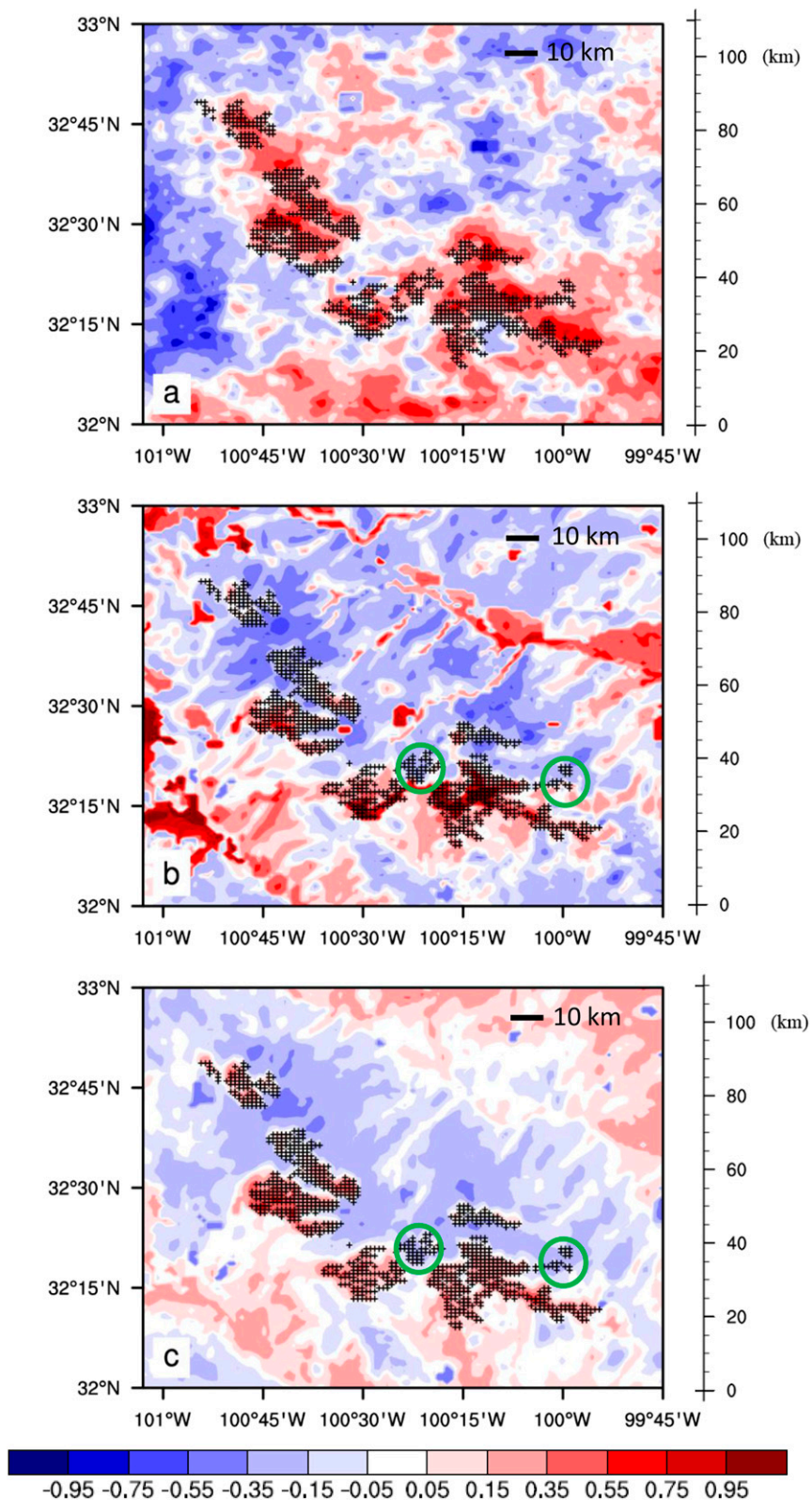


FIG. 7. July nighttime LST ($^{\circ}\text{C}$) differences between the post- and preturbine periods (2010–14 averages minus 2003–04 averages): (a) LST changes from MODIS observations, (b) LST changes from the 3Day simulations in EXP1, and (c) LST changes from the CON simulations in EXP1. The black dots indicate WFPs and the green circles indicate the location of WFPs built during the preturbine period. The MODIS nighttime LST is averaged from the two nighttime measurements at ~ 2230 and ~ 0130 LT and the simulated nighttime LST is averaged from hourly model output between 2200 and 0200 LT.

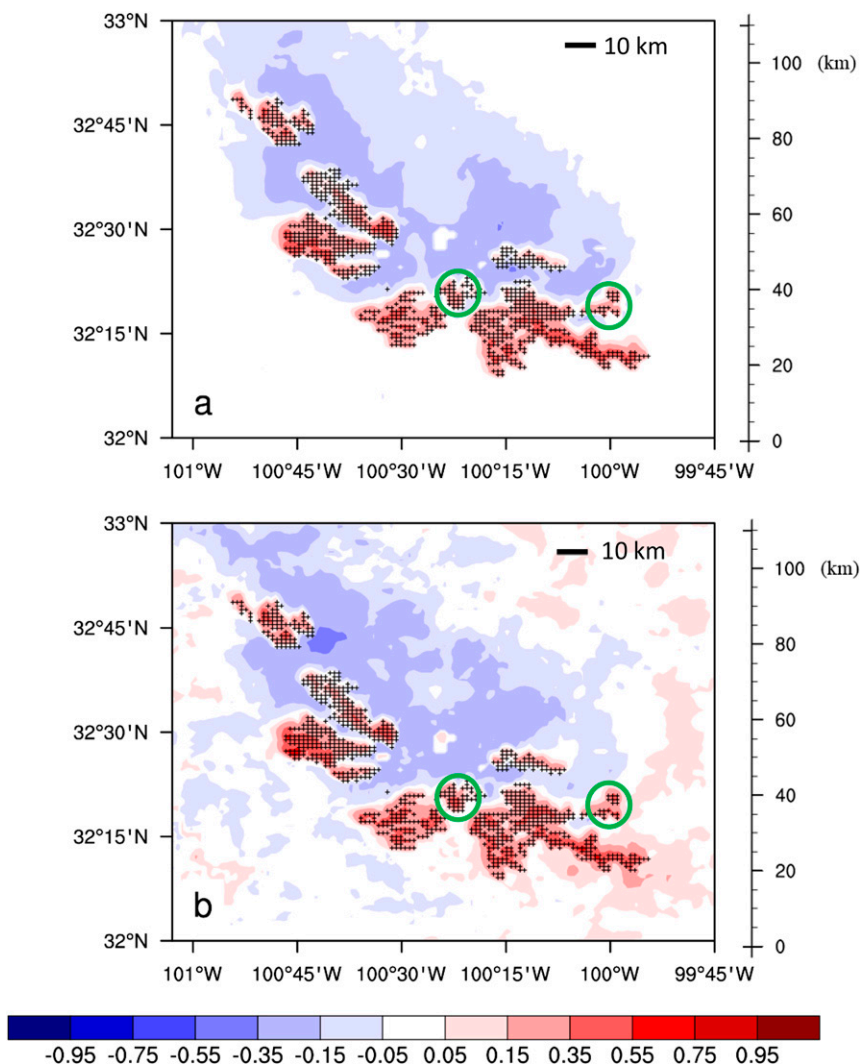


FIG. 8. July nighttime LST ($^{\circ}\text{C}$) differences between simulations with and without the wind turbine parameterization for the postturbine period (2010–14): (a) LST changes from the 3Day simulations in EXP2 and (b) LST changes from the CON simulations in EXP2. The black dots indicate WFPs and the green circles indicate the location of WFPs built during the preturbine period. The simulated nighttime LST is averaged from hourly model output between 2200 and 0200 LT.

at pixel levels, point out the model's potential of using the current wind turbine parameterization to assess real-world wind farm impacts at regional scales.

2) AREAL MEAN LST CHANGES

Using the predefined WFPs, DNWFPs, and UDWFPs, the areal mean LST changes are shown in Table 4. Over WFPs, the WRF Model produces a significant warming signal ($\sim 0.20^{\circ}\text{C}$) but the magnitude is about a tenth of degree smaller than the observations (0.33°C). As for DNWFPs, no significant changes (-0.06°C) are detected from the observations but a significant cooling signal is simulated (-0.15° to -0.20°C). Both MODIS and the

model show negligible temperature changes over the UNWFPs. Note that defining DNWFPs and UNWFPs even farther away (5 km) from the wind farm region do not change the results significantly. Overall, the spatial coupling and the magnitude of LST changes from EXP2 are more consistent with the MODIS observations than those from EXP1 mainly because we compare the LST differences between two different periods in EXP1, which contain more high-frequency signals (natural variability).

Our results indicate that the current wind turbine parameterization in the WRF Model has some difficulties in reproducing the observed LST variability at pixel

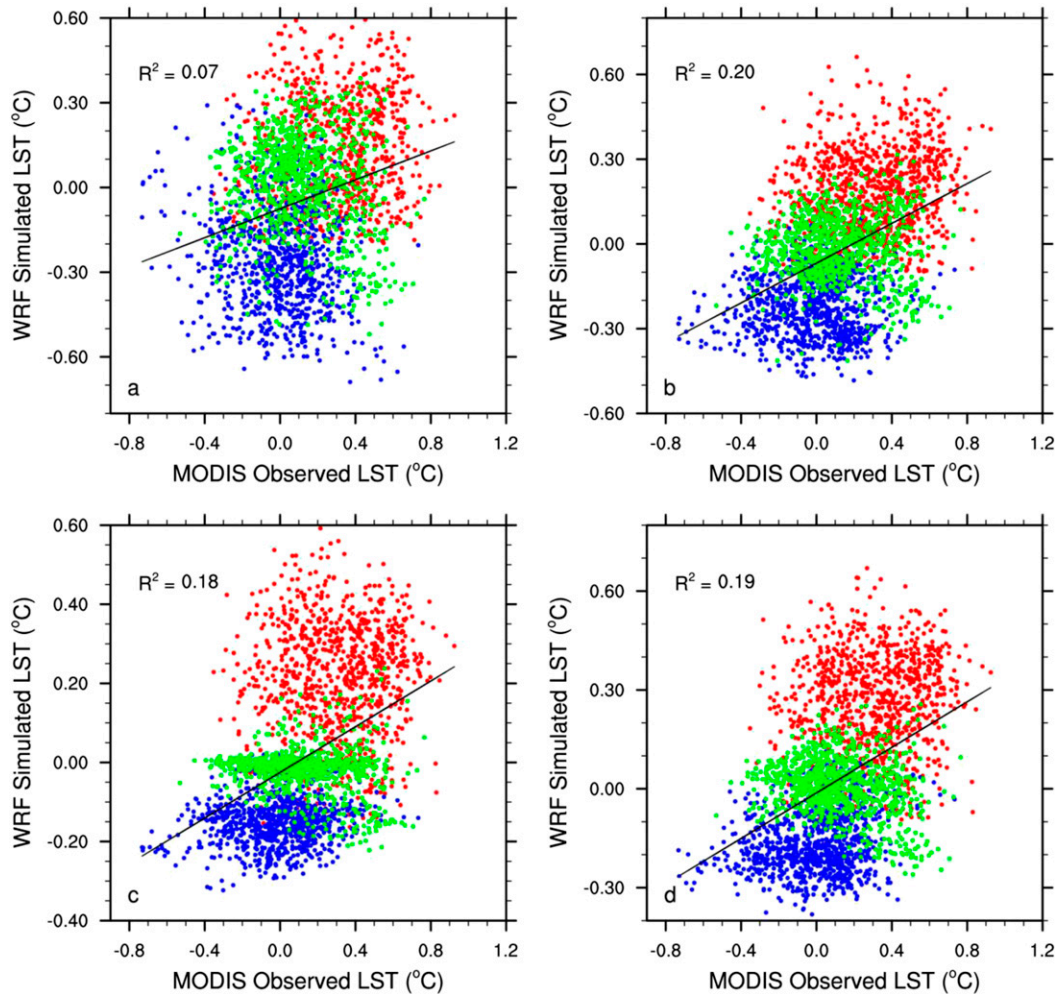


FIG. 9. Scatterplot of July nighttime LST ($^{\circ}\text{C}$) differences between MODIS and the WRF simulations (3Day and CON): (a) MODIS and 3Day from EXP1, (b) MODIS and CON from EXP1, (c) MODIS and 3Day from EXP2, and (d) MODIS and CON from EXP2. The red, green, and blue dots represent WFPs (917 pixels), DNWFPs (940 pixels), and UNWFPs (940 pixels), respectively; R^2 stands for the coefficient of determination and is computed from all 2797 pixels. The black line represents the best fitting using linear regression.

levels, but can capture the observed average warming anomalies at regional scales over WFPs although the simulated anomalies have a smaller magnitude than the MODIS observations. In contrast to the MODIS observations, the model also produces a significant surface cooling effect over DNWFPs.

e. Sensitivity tests to other possible factors

There are several other factors including topography, surface layer schemes, land surface models, and vertical resolution that may influence the simulated LST changes. We conduct sensitivity tests to confirm that the simulated wind farm-induced warming and cooling signals are robust. These tests cannot be performed in the manner as precisely as for EXP1 and EXP2 due to

lack of computer resources. Instead, we run a 3-day simulation from 30 June to 2 July 2011, and calculate the LST changes between 2200 and 0200 LT for the last two nights (the first day is treated as spinup). We choose these two nights (1–2 July 2011) as they are cloud free.

1) SENSITIVITY TO VARIATIONS IN TOPOGRAPHY

To test the role of topography in the down-wake cooling effect, we conducted simulations on three contrasting terrains (downslope, flat, and upslope) with 400 (20×20) artificial wind turbines (one turbine per pixel). Figures 10a–c indicate the geographical locations of the artificial wind turbines (black pixels) for these three terrains. Note that Figs. 10a and 10c share the similar topography. The distance between the wind farm in

TABLE 4. Areal mean LST changes (Δ LST, $^{\circ}$ C) of WFPs, DNWFPs, and UNWFPs for MODIS, 3Day, and CON simulations from EXP1 and EXP2. Areal mean LST changes in bold are statistically significant at the 10% level. (Note: The geographical locations of WFPs, DNWFPs, and UNWFPs are defined in Fig. 2b.)

Δ LST in EXP1: Postturbine (2010–14) LST minus preturbine (2003–04) LST			
	WFPs	DNWFPs	UNWFPs
Observation	0.33	−0.06	0.06
3Day	0.20	−0.15	0.01
CON	0.20	−0.20	−0.01
Δ LST in EXP2: Postturbine (2010–14) LST with wind turbines minus postturbine (2010–14) LST without wind turbines			
3Day	0.23	−0.15	−0.02
CON	0.26	−0.16	−0.01

Figs. 10a and 10b is about 100 km. Figures 10d–f show the spatial pattern of the LST changes with and without the wind turbine parameterization for these three experiments. Evidently, the pattern and magnitude of the cooling signals from these experiments are very similar, indicating that the variations of topography are not the primary factor for creating the downwind cooling signal. Over the artificial wind farm region, the warming signal is spatially coupled with the wind turbine location in all three experiments. However, the averaged warming signal varies: 0.23° C in Fig. 10d, 0.55° C in Fig. 10e, and 0.36° C in Fig. 10f, possibly due to the differences in elevation and land surface properties (e.g., land cover, soil moisture, and vegetation type/amount). Based on these results and the observational study of Zhou et al. (2013b), we believe that the variation in topography is not the major cause of the simulated down-wake cooling effect.

2) SENSITIVITY TO SURFACE LAYER SCHEMES AND LAND SURFACE MODELS

To explore the sensitivity of the model LST biases and simulated changes to the choice of surface layer schemes and the land surface models, we choose two land surface models [Noah (Chen and Dudhia 2001) and Noah-MP (Niu et al. 2011)] and two surface layer schemes [Revised MM5 Monin–Obukhov (MO; Jiménez et al. 2012) and MYNN (Nakanishi and Niino 2009)] to conduct our experiments. In total, there are four combinations: 1) NoahMP-MYNN, 2) NoahMP-MO, 3) Noah-MYNN, and 4) Noah-MO. We also analyze the daily MODIS images for 1–2 July 2011 as observations.

Figure 11a shows the spatial pattern of the background LST from the MODIS observations while Figs. 11b–e are that from each combination. Clearly, the WRF Model creates a warm bias over the study region, despite different combinations of surface layer schemes and land surface models. Therefore, we believe that the model’s warm bias is systematic and independent on the choice of surface layer schemes or land surface models.

Moreover, similar nighttime warm biases have been documented in recent studies (Liu et al. 2017; Chen et al. 2014) as well. Both studies used Noah-MP as the land surface model but different initialization datasets (ERA-Interim and CFSR). Although the temporal and spatial scales in their simulations are different from this study, the summer nighttime near-surface (2 m) warm bias over Texas is evident. However, neither of these two studies provides any reasoning for why this warm bias occurs. To further examine this warm bias, we compare the observed 2-m air temperature from the same field campaign site with the model simulations and find similar warm bias (figure not shown). Understanding the cause for this warm bias is beyond the scope of this study but the uncertainties associated with it are addressed in section 3e.

Figure 12 shows the spatial pattern of the LST changes from our four experiments. The spatial pattern of LST changes (warming and cooling signals) exhibit very similar features among the four plots. There is surface warming over the wind farm region and surface cooling behind the wind farm region. However, Noah-MO seems to produce a weaker LST response as compared to the other three experiments. For example, the areal mean warming and cooling signals in Fig. 12d are less significant ($\sim 0.1^{\circ}$ C) as compared to Figs. 12a–c. Overall, this small temperature difference due to different surface layer schemes and land surface models has little impact on the main conclusions of this work, that is the current WRF wind turbine parameterization tends to underestimate the observed surface warming signal and produce a downwind cooling signal that have not been observed.

3) SENSITIVITY TO VERTICAL RESOLUTION

The sensitivity of our results to vertical resolution is tested by conducting an additional experiment with 59 vertical layers (20 layers below 200 m). Figures 13a and 13b indicate the spatial pattern of the LST changes with 39 vertical levels (used in this study) and 59 vertical levels, respectively. Increasing the vertical resolution reduces the

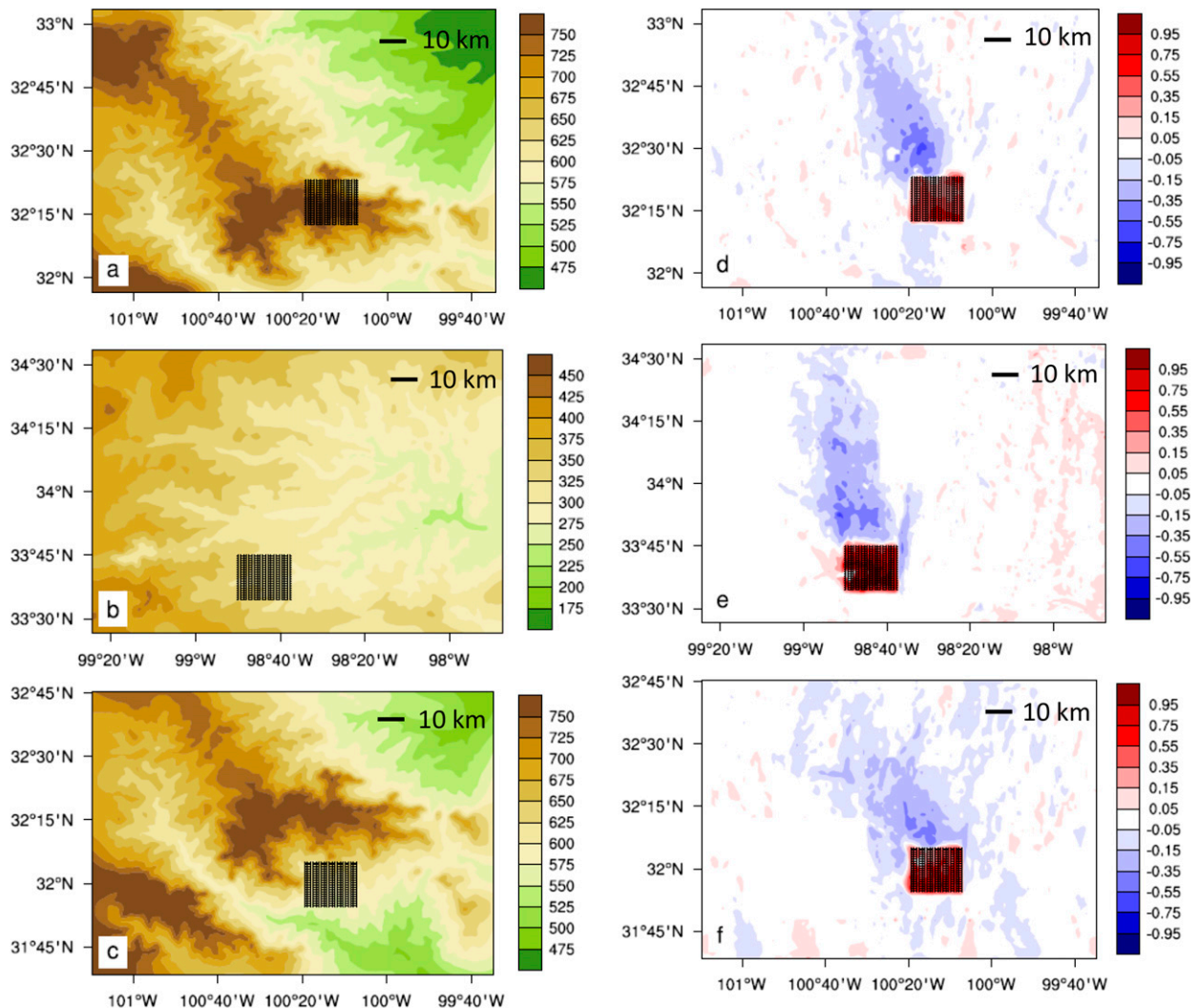


FIG. 10. Spatial pattern of terrain elevation (m) and nighttime LST ($^{\circ}\text{C}$) differences between simulations with and without the wind turbine parameterization for 1–2 Jul 2011 used to test the sensitivity of wind farm–induced cooling signals to variations in topography: (a) Elevation map of the downslope terrain, (b) elevation map of the flat terrain, (c) elevation map of the upslope flat terrain, (d) LST changes for the downslope terrain, (e) LST changes for the flat terrain, and (f) LST changes for the upslope terrain. The black dots mark the locations of 400 (20×20) artificial wind turbines. The simulated nighttime LST change is averaged from hourly model output between 2200 and 0200 LT.

areal warming signals over WFPs by 0.05°C but enhances the areal cooling signal over DNWFPs by 0.15°C . Similar to the above sensitivity tests, these small changes in temperature have little influence on our main conclusions.

4. Uncertainties

Zhou et al. (2013a,b) extensively discussed the data uncertainties associated with the MODIS LST and found that such uncertainties cannot explain the observed warming signal over the wind farms. Here we will discuss modeling uncertainties that are not addressed in the previous studies.

The wind farm–induced LST signal is detected based on MODIS observations under cloud-free conditions. To make the comparison between the WRF simulations and MODIS data meaningful, we calculate the CLWP to represent CC and use the percentage of cloud-covered pixels over the wind farm region and its immediate vicinity as a threshold to decide whether it is a cloudy or cloud-free day. A sensitivity test is conducted by increasing or decreasing the threshold of cloud-covered pixels (by an interval of 5%) but no change on the classification of the number of cloud-free days is found. In addition, cloud-free days are defined at the pixel-level in MODIS but at the regional level in the simulations.

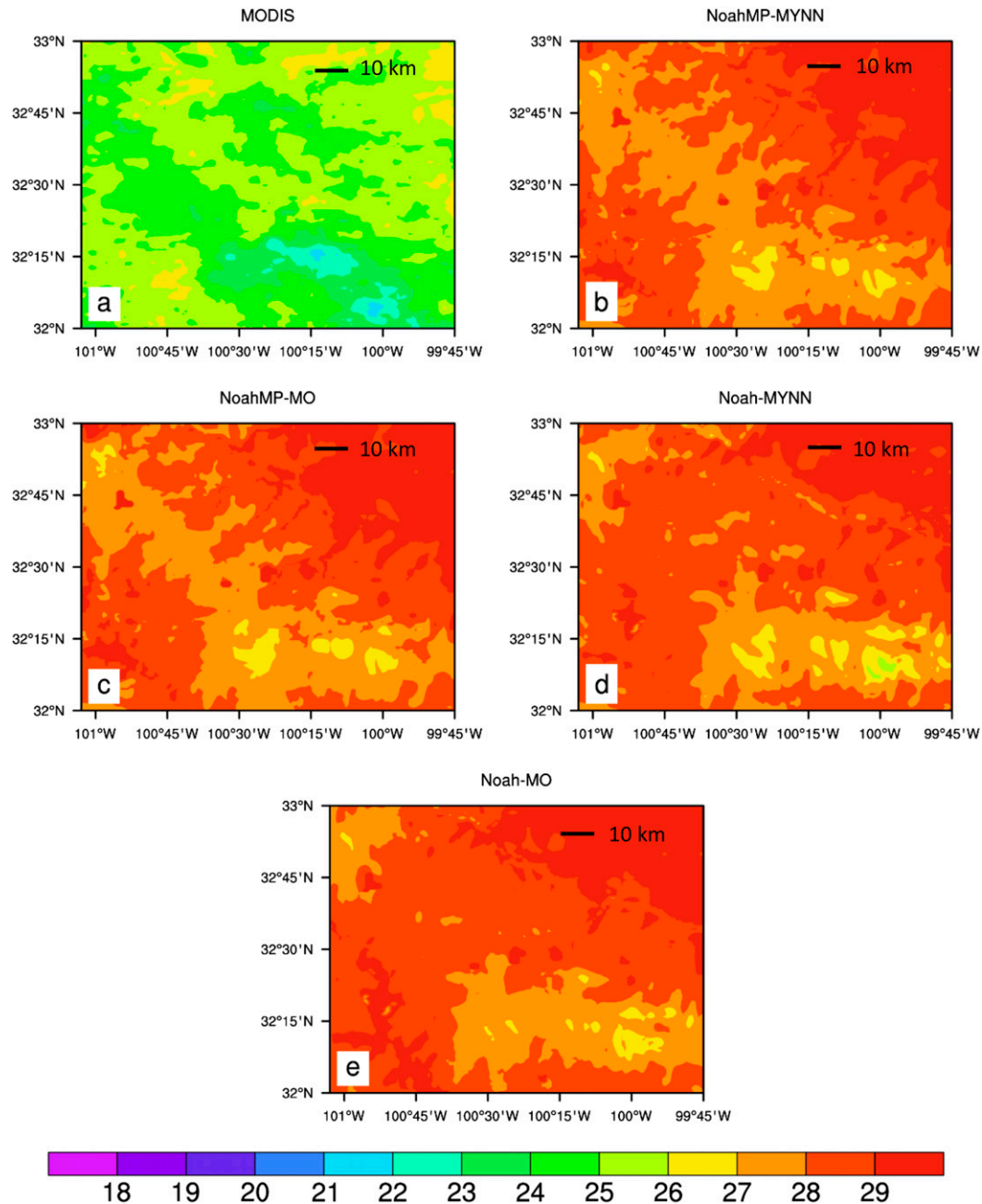


FIG. 11. Spatial pattern of background nighttime LST ($^{\circ}\text{C}$) for 1–2 Jul 2011 used to test the sensitivity of the simulated LST warm bias to land surface models and surface layer schemes: (a) MODIS, (b) NoahMP-MYNN, (c) NoahMP-MO, (d) Noah-MYNN, and (e) Noah-MO. The MODIS nighttime LST is averaged from the two nighttime measurements at ~ 2230 and ~ 0130 LT and the simulated nighttime LST is averaged from hourly model output between 2200 and 0200 LT.

The differences in cloud treatments between MODIS and our methodology could introduce some uncertainties to our results.

The model output is saved at hourly frequency. Hence, there is no exact time output from our simulations to match MODIS measurements. The simulated

nighttime LST used for our analysis is the 5-h average from 2200 to 0200 LT whereas the MODIS nighttime LST is the average of two observations at ~ 2230 and ~ 0130 LT. Our sensitivity tests using the hourly output averaged between 2200 and 2300 LT (corresponding to the ~ 2230 LT MODIS measurement time) and between

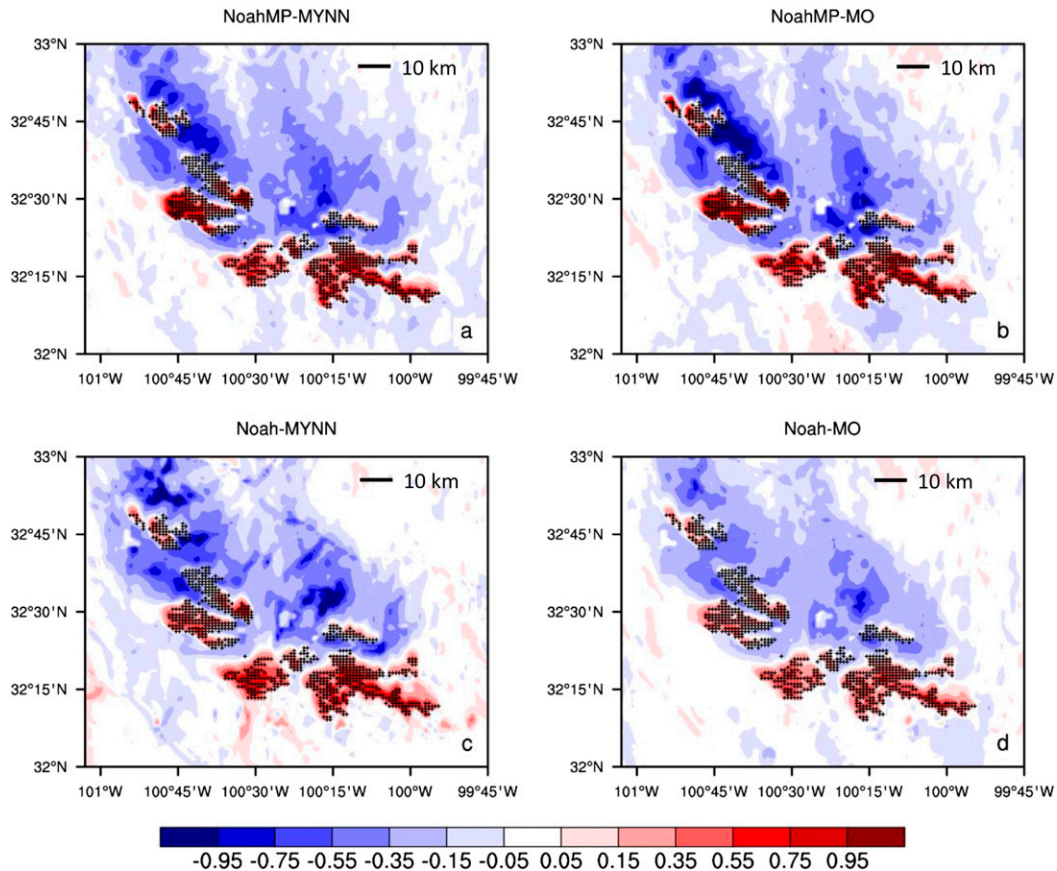


FIG. 12. Nighttime LST ($^{\circ}\text{C}$) differences between simulations with and without the wind turbine parameterization for 1–2 Jul 2011 used to test the sensitivity of the simulated surface warming and cooling signals to land surface models and surface layer schemes: (a) NoahMP-MYNN, (b) NoahMP-MO, (c) Noah-MYNN, and (d) Noah-MO. The black dots indicate WFPs.

0100 and 0200 LT (corresponding to the \sim 0130 LT MODIS measurement time) indicate negligible differences from the 5-h average.

The systematic warm bias of the background LST is expected to have a small impact on our conclusions as we compare the LST differences between the control and experiment runs, which cancel most of the model's systematic warm bias. However, possibly it could potentially impact the model stability and the wind turbines performance (Barthelmie and Jensen 2010; Peña and Rathmann 2014; Abkar and Porté-Agel 2015), and thus to some extent, affect the simulated LST changes both over the wind farm regions and the downwind areas.

The simulated wind farm impact on LST differs between the CON and 3Day runs, especially in EXP1, but it is difficult to quantify which one is better in simulating wind farm impacts as both have limitations (see more in the introduction). Further attribution of the difference between the CON and 3Day runs is beyond the scope of this study, but future studies should be aware of such

initialization uncertainties and limitations when conducting wind farm simulations using the WRF Model.

Wind validation with the sodar observations is only conducted for July 2012 because of the lack of wind observations. To further confirm whether the low wind speed bias is true, we conduct additional model simulations for August 2012 when a full month of sodar observations are available and reach the same conclusion (see online supplemental Fig. S2). This suggests that the WRF Model most likely overestimates the turbine-induced LST changes over our study region because of over-predicted wind speed. Previous studies suggest that the wind speed biases between observed and simulated are often seen over land because of issues with the representativeness of the mesoscale grid (Rife et al. 2004), errors in the model-assigned surface roughness length, and elevation (Horvath et al. 2012; Santos-Alamillos et al. 2013; Badger et al. 2014). However, the attribution of the wind biases to these factors is beyond the scope of this article. Note that we cannot validate the simulated wind

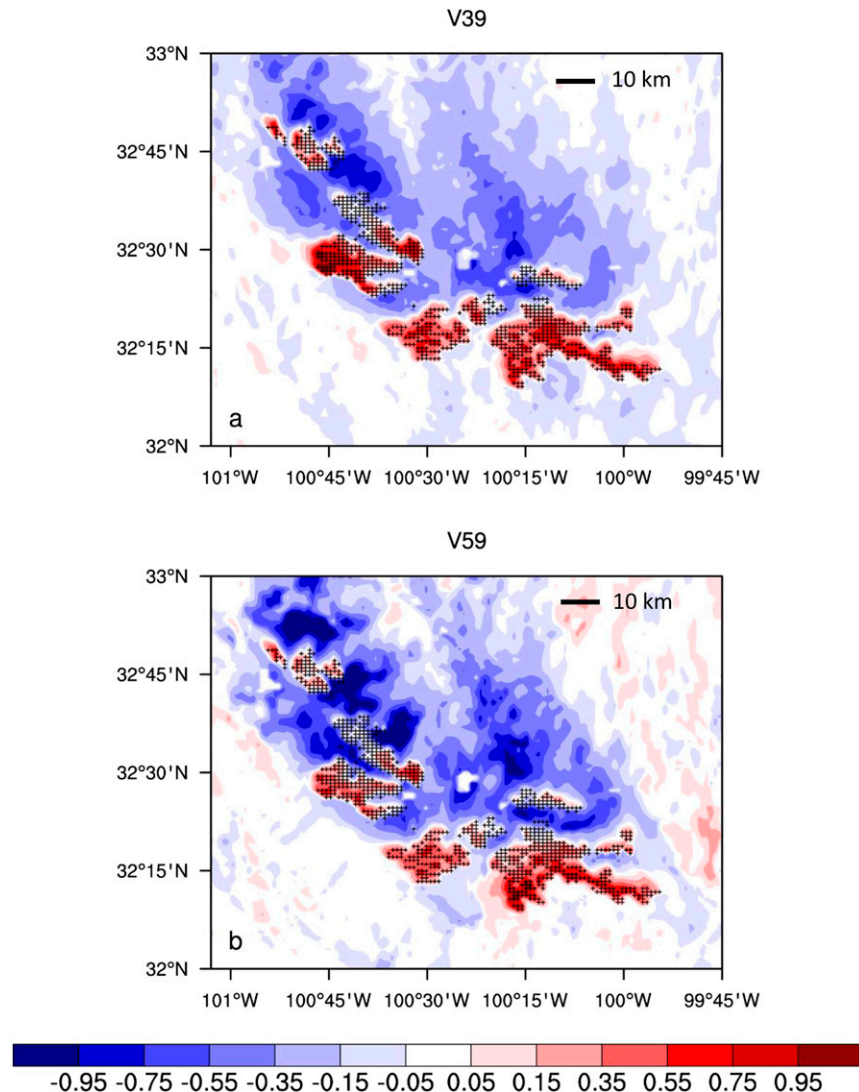


FIG. 13. Nighttime LST ($^{\circ}\text{C}$) differences between simulations with and without the wind turbine parameterization for 1–2 Jul 2011 used to test the sensitivity of the simulated surface warming and cooling signals to the vertical resolution of the WRF simulations: (a) 39 vertical levels (10 layers below 200 m) and (b) 59 vertical levels (20 layers below 200 m). The black dots indicate WFPs.

conditions for other July months because there are no sodar observations available. Moreover, there are multiple wind turbines in one grid point (85.2% of the WFPs have two or more wind turbines) and the model does not take into account the fact that some of the wind turbines, in reality, will be down for repair or maintenance, which could also lead to a slight overprediction of the simulated turbine impacts. However, if these factors were considered, the simulated turbine-induced warming signals over WFPs would be even smaller.

Our simulations indicate a significant anomalous cooling effect over the wind farm wake region in the downwind direction. However, this far downwind (40 km) cooling

effect has not been detected from previous field campaigns and satellite observations. Note that [Fitch et al. \(2013b\)](#) also produce near-surface (2 m) cooling effects at nighttime in their idealized simulations. Together, this may point to some possible limitations of the current wind turbine parameterization, which deserve further attention and observational validation.

5. Conclusions

This research examines the WRF Model's ability in simulating WF impact on LST by conducting real-world wind farm experiments driven by realistic initial and

boundary conditions. Two groups of experiments are conducted over west-central Texas for the month of July for 7 years (2003–04 and 2010–14) and are compared with the observations from MODIS and the first Wind Forecast Improvement Project (WFIP) field campaign. The first group directly compares the simulated LST changes between the pre- and postturbine periods with MODIS observations to assess the model's ability to simulate the observed wind farm impact on LST. The second group is a controlled experiment to directly assess the sensitivity of the simulated LST to the wind turbine parameterization by examining the LST differences with and without the presence of wind turbines for the postturbine period. For each group, both continuous (CON) and 3-day reinitialized (3Day) simulations are considered. Overall, the WRF Model reproduces the observed spatiotemporal variations of the background LST moderately well but has difficulties in reproducing such variations for the turbine-induced LST change signals at pixel levels. However, the model is still able to reproduce the coherent and consistent responses of the observed LST changes at regional scales. The wind farm-induced LST warming signals from the current WRF wind turbine parameterization agree well with the satellite observations in terms of their spatial coupling with the wind farm layout. The simulated areal mean wind farm impact on LST over the WFPs (0.20° – 0.26°C) is about a tenth of degree smaller than that from MODIS (0.33°C). However, our results also suggest that the current wind turbine parameterization tends to induce a cooling effect downwind of the wind farm region at nighttime, which has not been confirmed by any previous field campaigns and satellite observations. Numerous experiments are performed to test the sensitivity of our results to several factors (e.g., topography variations, scheme dependency, and vertical resolution) and show negligible impacts on the above conclusions. Note that the surface warming (or cooling) from both the MODIS observations and model simulations represent a redistribution of heat in the atmosphere, not actual heating of the atmosphere by the turbines.

This study marks a major improvement over an earlier effort (Cervarich et al. 2013) to simulate observed LST changes due to operating wind farms. This improvement occurs for three reasons. First, we compare the simulated LST only for the cloud-free days to be consistent with MODIS observations. Second, we use a multiyear average approach to better isolate the low-frequency wind farm-induced LST signal from the background high-frequency LST variations. This strategy is similar to the spatial and temporal averaging approaches used effectively in observations to obtain the wind farm signals (Zhou et al. 2012, 2013a). Third, we use the sensitivity test

in EXP2 to further quantify the simulated wind farms effects in a controlled manner by switching the turbine parameterization on and off.

One possible reason for the simulated cooling effect over the wind farm wake region is that the current wind turbine parameterization has deficiencies in simulating the wake processes. Hence, validating and potentially improving the wind turbine representation for mesoscale models should be a priority. A better wind turbine parameterization will improve the simulation of not only temperature but also wind speed and power production, thereby meeting a critical need for the wind energy industry. Unfortunately, data on turbulent processes in the wake of wind farms are scarce because most field campaigns are conducted within and in the immediate vicinity of wind farms. Hence, more comprehensive field campaigns are needed to study wind farm–ABL interactions, and more measurements (heat and momentum fluxes) over the wind farm wake region are needed to validate and improve parameterizations of wind turbines in numerical models.

The present paper focuses on validation of the current wind turbine parameterization in simulating the real-world wind farm impact on LST at the regional scales. Uncovering physical processes behind the simulated warming and cooling signals requires an extensive analysis of changes in the surface energy budget, variations of vertical profiles of temperature as well as turbulent fluxes of heat and momentum over the wind farms and their wake regions. It will be detailed in another paper, which will be beneficial for improving the current wind turbine parameterization and understanding the physical mechanisms for the wind farm-induced LST changes.

Acknowledgments. The authors are thankful to Dr. Sven Schmitz and his research group at The Pennsylvania State University for generously providing turbine blade specifications of the PSU Generic 1.5-MW turbine. We also would like to thank three anonymous reviewers for their helpful comments. This work was supported by National Science Foundation Grant NSF-AGS-1247137.

REFERENCES

- Abkar, M., and F. Porté-Agel, 2015: Influence of atmospheric stability on wind-turbine wakes: A large-eddy simulation study. *Phys. Fluids*, **27**, 035104, <https://doi.org/10.1063/1.4913695>.
- Armstrong, A., S. Waldron, J. Whitaker, and N. J. Ostle, 2014: Wind farm and solar park effects on plant–soil carbon cycling: Uncertain impacts of changes in ground-level microclimate. *Global Change Biol.*, **20**, 1699–1706, <https://doi.org/10.1111/gcb.12437>.
- AWEA, 2015: U.S. wind industry annual market report. American Wind Energy Association, 110 pp., <http://www.awea.org/Resources/Content.aspx?ItemNumber=875&navItemNumber=621>.

- Badger, J., H. P. Frank, A. N. Hahmann, and G. Giebel, 2014: Wind-climate estimation based on mesoscale and microscale modeling: Statistical–dynamical downscaling for wind energy applications. *J. Appl. Meteor. Climatol.*, **53**, 1901–1919, <https://doi.org/10.1175/JAMC-D-13-0147.1>.
- Baidya Roy, S., 2011: Simulating impacts of wind farms on local hydrometeorology. *J. Wind Eng. Ind. Aerodyn.*, **99**, 491–498, <https://doi.org/10.1016/j.jweia.2010.12.013>.
- , and J. J. Traiteur, 2010: Impacts of wind farms on surface air temperatures. *Proc. Natl. Acad. Sci. USA*, **107**, 17 899–17 904, <https://doi.org/10.1073/pnas.1000493107>.
- , S. W. Pacala, and R. L. Walko, 2004: Can large wind farms affect local meteorology? *J. Geophys. Res.*, **109**, D19101, <https://doi.org/10.1029/2004JD004763>.
- Barrie, D. B., and D. B. Kirk-Davidoff, 2010: Weather response to a large wind turbine array. *Atmos. Chem. Phys.*, **10**, 769–775, <https://doi.org/10.5194/acp-10-769-2010>.
- Barthelmie, R. J., and L. E. Jensen, 2010: Evaluation of wind farm efficiency and wind turbine wakes at the Nysted offshore wind farm. *Wind Energy*, **13**, 573–586, <https://doi.org/10.1002/we.408>.
- Cal, R. B., J. Lebrón, L. Castillo, H. S. Kang, and C. Meneveau, 2010: Experimental study of the horizontally averaged flow structure in a model wind-turbine array boundary layer. *J. Renewable Sustainable Energy*, **2**, 013106, <https://doi.org/10.1063/1.3289735>.
- Calaf, M., C. Meneveau, and J. Meyers, 2010: Large eddy simulation study of fully developed wind-turbine array boundary layers. *Phys. Fluids*, **22**, 015110, <https://doi.org/10.1063/1.3291077>.
- , M. B. Parlange, and C. Meneveau, 2011: Large eddy simulation study of scalar transport in fully developed wind-turbine array boundary layers. *Phys. Fluids*, **23**, 126603, <https://doi.org/10.1063/1.3663376>.
- Cervarich, M. C., S. Baidya Roy, and L. Zhou, 2013: Spatiotemporal structure of wind farm-atmospheric boundary layer interactions. *Energy Procedia*, **40**, 530–536, <https://doi.org/10.1016/j.egypro.2013.08.061>.
- Chang, R., R. Zhu, and P. Guo, 2016: A case study of land-surface-temperature impact from large-scale deployment of wind farms in China from Guazhou. *Remote Sens.*, **8**, 790, <https://doi.org/10.3390/rs8100790>.
- Chen, F., and J. Dudhia, 2001: Coupling an advanced land surface–hydrology model with the Penn State–NCAR MM5 modeling system. Part I: Model implementation and sensitivity. *Mon. Wea. Rev.*, **129**, 569–585, [https://doi.org/10.1175/1520-0493\(2001\)129<0569:CAALSH>2.0.CO;2](https://doi.org/10.1175/1520-0493(2001)129<0569:CAALSH>2.0.CO;2).
- , C. Liu, J. Dudhia, and M. Chen, 2014: A sensitivity study of high-resolution regional climate simulations to three land surface models over the western United States. *J. Geophys. Res. Atmos.*, **119**, 7271–7291, <https://doi.org/10.1002/2014JD021827>.
- Churchfield, M. J., S. Lee, J. Michalakes, and P. J. Moriarty, 2012: A numerical study of the effects of atmospheric and wake turbulence on wind turbine dynamics. *J. Turbul.*, **13**, N14, <https://doi.org/10.1080/14685248.2012.668191>.
- Conil, S., and A. Hall, 2006: Local regimes of atmospheric variability: A case study of southern California. *J. Climate*, **19**, 4308–4325, <https://doi.org/10.1175/JCLI3837.1>.
- Creech, A., W. G. Früh, and A. E. Maguire, 2015: Simulations of an offshore wind farm using large-eddy simulation and a torque-controlled actuator disc model. *Surv. Geophys.*, **36**, 427–481, <https://doi.org/10.1007/s10712-015-9313-7>.
- Dudhia, J., 1989: Numerical study of convection observed during the winter monsoon experiment using a mesoscale two-dimensional model. *J. Atmos. Sci.*, **46**, 3077–3107, [https://doi.org/10.1175/1520-0469\(1989\)046<3077:NSOCOD>2.0.CO;2](https://doi.org/10.1175/1520-0469(1989)046<3077:NSOCOD>2.0.CO;2).
- Fitch, A. C., 2015: Climate impacts of large-scale wind farms as parameterized in a global climate model. *J. Climate*, **28**, 6160–6180, <https://doi.org/10.1175/JCLI-D-14-00245.1>.
- , J. Olson, J. Lundquist, J. Dudhia, A. Gupta, J. Michalakes, and I. Barstad, 2012: Local and mesoscale impacts of wind farms as parameterized in a mesoscale NWP model. *Mon. Wea. Rev.*, **140**, 3017–3038, <https://doi.org/10.1175/MWR-D-11-00352.1>.
- , J. K. Lundquist, and J. B. Olson, 2013a: Mesoscale influences of wind farms throughout a diurnal cycle. *Mon. Wea. Rev.*, **141**, 2173–2198, <https://doi.org/10.1175/MWR-D-12-00185.1>.
- , J. B. Olson, and J. K. Lundquist, 2013b: Parameterization of wind farms in climate models. *J. Climate*, **26**, 6439–6458, <https://doi.org/10.1175/JCLI-D-12-00376.1>.
- Freedman, J. M., and Coauthors, 2014: The Wind Forecast Improvement Project (WFIP): A public/private partnership for improving short term wind energy forecasts and quantifying the benefits of utility operations—The southern study area. AWS Truepower Tech. Rep. DOE-AWST-04420, U.S. DOE Office of Energy Efficiency and Renewable Energy (EERE), Wind and Hydropower Technology Program (EE-2B), 107 pp., <https://doi.org/10.2172/1129905>.
- Harris, R. A., L. Zhou, and G. Xia, 2014: Satellite observations of wind farm impacts on nocturnal land surface temperature in Iowa. *Remote Sens.*, **6**, 12 234–12 246, <https://doi.org/10.3390/rs61212234>.
- Hong, S. Y., J. Dudhia, and S. H. Chen, 2004: A revised approach to ice microphysical processes for the bulk parameterization of clouds and precipitation. *Mon. Wea. Rev.*, **132**, 103–120, [https://doi.org/10.1175/1520-0493\(2004\)132<0103:ARATIM>2.0.CO;2](https://doi.org/10.1175/1520-0493(2004)132<0103:ARATIM>2.0.CO;2).
- Horvath, K., D. Koracin, R. Vellore, J. Jiang, and R. Belu, 2012: Sub-kilometer dynamical downscaling of near-surface winds in complex terrain using WRF and MM5 mesoscale models. *J. Geophys. Res.*, **117**, D11111, <https://doi.org/10.1029/2012JD017432>.
- Jiménez, P. A., J. F. González-Rouco, E. García-Bustamante, J. Navarro, J. P. Montávez, J. V. de Arellano, J. Dudhia, and A. Muñoz-Roldan, 2010: Surface wind regionalization over complex terrain: Evaluation and analysis of a high-resolution WRF simulation. *J. Appl. Meteor. Climatol.*, **49**, 268–287, <https://doi.org/10.1175/2009JAMC2175.1>.
- , J. Dudhia, J. F. González-Rouco, J. Navarro, J. P. Montávez, and E. García-Bustamante, 2012: A revised scheme for the WRF surface layer formulation. *Mon. Wea. Rev.*, **140**, 898–918, <https://doi.org/10.1175/MWR-D-11-00056.1>.
- , J. Navarro, A. M. Palomares, and J. Dudhia, 2015: Mesoscale modeling of offshore wind turbine wakes at the wind farm resolving scale: A composite-based analysis with the Weather Research and Forecasting model over Horns Rev. *Wind Energy*, **18**, 559–566, <https://doi.org/10.1002/we.1708>.
- Kain, J. S., 2004: The Kain–Fritsch convective parameterization: An update. *J. Appl. Meteor.*, **43**, 170–181, [https://doi.org/10.1175/1520-0450\(2004\)043<0170:TKCPAU>2.0.CO;2](https://doi.org/10.1175/1520-0450(2004)043<0170:TKCPAU>2.0.CO;2).
- Keith, D. W., J. DeCarolis, D. Denkenberger, D. Lenschow, S. L. Malyshev, S. Pacala, and P. J. Rasch, 2004: The influence of large-scale wind power on global climate. *Proc. Natl. Acad. Sci. USA*, **101**, 16 115–16 120, <https://doi.org/10.1073/pnas.0406930101>.

- Kirk-Davidoff, D. B., and D. W. Keith, 2008: On the climate impact of surface roughness anomalies. *J. Atmos. Sci.*, **65**, 2215–2234, <https://doi.org/10.1175/2007JAS2509.1>.
- Liu, C., and Coauthors, 2017: Continental-scale convection-permitting modeling of the current and future climate of North America. *Climate Dyn.*, **49**, 71–95, <https://doi.org/10.1007/s00382-016-3327-9>.
- Lo, J. C. F., Z.-L. Yang, and R. A. Pielke, 2008: Assessment of three dynamical climate downscaling methods using the Weather Research and Forecasting (WRF) model. *J. Geophys. Res.*, **113**, D09112, <https://doi.org/10.1029/2007JD009216>.
- Lu, H., and F. Porté-Agel, 2011: Large-eddy simulation of a very large wind farm in a stable atmospheric boundary layer. *Phys. Fluids*, **23**, 065101, <https://doi.org/10.1063/1.3589857>.
- Mellor, G. L., and T. Yamada, 1982: Development of a turbulence closure model for geophysical fluid problems. *Rev. Geophys.*, **20**, 851–875, <https://doi.org/10.1029/RG020i004p00851>.
- Mirocha, J. D., B. Kosovic, M. L. Aitken, and J. K. Lundquist, 2014: Implementation of a generalized actuator disk wind turbine model into the weather research and forecasting model for large-eddy simulation applications. *J. Renewable Sustainable Energy*, **6**, 013104, <https://doi.org/10.1063/1.4861061>.
- Mlawer, E. J., S. J. Taubman, P. D. Brown, M. J. Iacono, and S. A. Clough, 1997: Radiative transfer for inhomogeneous atmosphere: RRTM, a validated correlated-k model for the longwave. *J. Geophys. Res.*, **102**, 16 663–16 682, <https://doi.org/10.1029/97JD00237>.
- Nakanishi, M., and H. Niino, 2009: Development of an improved turbulence closure model for the atmospheric boundary layer. *J. Meteor. Soc. Japan*, **87**, 895–912, <https://doi.org/10.2151/jmsj.87.895>.
- Niu, G. Y., and Coauthors, 2011: The community Noah land surface model with multiparameterization options (Noah-MP): 1. Model description and evaluation with local-scale measurements. *J. Geophys. Res.*, **116**, D12109, <https://doi.org/10.1029/2010JD015139>.
- Pan, Z., E. Takle, W. Gutowski, and R. Turner, 1999: Long simulation of regional climate as a sequence of short segments. *Mon. Wea. Rev.*, **127**, 308–321, [https://doi.org/10.1175/1520-0493\(1999\)127<0308:LSORCA>2.0.CO;2](https://doi.org/10.1175/1520-0493(1999)127<0308:LSORCA>2.0.CO;2).
- Peña, A., and O. Rathmann, 2014: Atmospheric stability-dependent infinite wind-farm models and the wake-decay coefficient. *Wind Energy*, **17**, 1269–1285, <https://doi.org/10.1002/we.1632>.
- Porté-Agel, F., Y. T. Wu, H. Lu, and R. J. Conzemius, 2011: Large-eddy simulation of atmospheric boundary layer flow through wind turbines and wind farms. *J. Wind Eng. Ind. Aerodyn.*, **99**, 154–168, <https://doi.org/10.1016/j.jweia.2011.01.011>.
- Qian, J. H., A. Seth, and S. Zebiak, 2003: Reinitialized versus continuous simulations for regional climate downscaling. *Mon. Wea. Rev.*, **131**, 2857–2874, [https://doi.org/10.1175/1520-0493\(2003\)131<2857:RVCSFR>2.0.CO;2](https://doi.org/10.1175/1520-0493(2003)131<2857:RVCSFR>2.0.CO;2).
- Rajewski, D. A., and Coauthors, 2013: Crop Wind Energy Experiment (CWEX): Observations of surface-layer, boundary layer, and mesoscale interactions with a wind farm. *Bull. Amer. Meteor. Soc.*, **94**, 655–672, <https://doi.org/10.1175/BAMS-D-11-00240.1>.
- , E. S. Takle, J. K. Lundquist, J. H. Prueger, R. L. Pfeiffer, J. L. Hatfield, K. Spoth, and R. K. Doorenbos, 2014: Changes in fluxes of heat, H₂O, and CO₂ caused by a large wind farm. *Agric. For. Meteorol.*, **194**, 175–187, <https://doi.org/10.1016/j.agrformet.2014.03.023>.
- , —, J. H. Prueger, and R. K. Doorenbos, 2016: Toward understanding the physical link between turbines and microclimate impacts from in situ measurements in a large wind farm. *J. Geophys. Res. Atmos.*, **121**, 13 392–13 414, <https://doi.org/10.1002/2016JD025297>.
- Rife, D. L., C. A. Davis, Y. Liu, and T. T. Warner, 2004: Predictability of low-level winds by mesoscale meteorological models. *Mon. Wea. Rev.*, **132**, 2553–2569, <https://doi.org/10.1175/MWR2801.1>.
- Santos-Alamillos, F. J., D. Pozo-Vázquez, J. A. Ruiz-Arias, V. Lara-Fanego, and J. Tovar-Pescador, 2013: Analysis of WRF Model wind estimate sensitivity to physics parameterization choice and terrain representation in Andalusia (southern Spain). *J. Appl. Meteor. Climatol.*, **52**, 1592–1609, <https://doi.org/10.1175/JAMC-D-12-0204.1>.
- Schmitz, S., 2012: XTURB-PSU: A wind turbine design and analysis tool, version 1.1. Dept. of Aerospace Engineering, The Pennsylvania State University, accessed 10 February 2017, http://www.aero.psu.edu/Faculty_Staff/schmitz/XTurb/XTurb.html.
- Skamarock, W. C., and J. B. Klemp, 2008: A time-split non-hydrostatic atmospheric model for weather research and forecasting applications. *J. Comput. Phys.*, **227**, 3465–3485, <https://doi.org/10.1016/j.jcp.2007.01.037>.
- Slawsky, L. M., L. Zhou, S. Baidya Roy, G. Xia, M. Vuille, and R. A. Harris, 2015: Observed thermal impacts of wind farms over northern Illinois. *Sensors*, **15**, 14 981–15 005, <https://doi.org/10.3390/s150714981>.
- Smith, C. M., R. J. Barthelmie, and S. C. Pryor, 2013: In situ observations of the influence of a large onshore wind farm on near-surface temperature, turbulence intensity and wind speed profiles. *Environ. Res. Lett.*, **8**, 034006, <https://doi.org/10.1088/1748-9326/8/3/034006>.
- Tang, B., D. Wu, X. Zhao, T. Zhou, W. Zhao, and H. Wei, 2017: The observed impacts of wind farms on local vegetation growth in northern China. *Remote Sens.*, **9**, 332, <https://doi.org/10.3390/rs9040332>.
- U.S. DOE, 2015: Wind vision: A new era for wind power in the United States. U. S. Dept. of Energy Rep. DOE/GO-102015-4557, 350 pp., https://energy.gov/sites/prod/files/2015/03/f20/wv_full_report.pdf.
- Wan, Z., 2002: Estimate of noise and systematic error in early thermal infrared data of the Moderate Resolution Imaging Spectroradiometer (MODIS). *Remote Sens. Environ.*, **80**, 47–54, [https://doi.org/10.1016/S0034-4257\(01\)00266-8](https://doi.org/10.1016/S0034-4257(01)00266-8).
- , 2008: New refinements and validation of the MODIS Land-Surface Temperature/Emissivity products. *Remote Sens. Environ.*, **112**, 59–74, <https://doi.org/10.1016/j.rse.2006.06.026>.
- Wang, C., and R. G. Prinn, 2010: Potential climatic impacts and reliability of very large-scale wind farms. *Atmos. Chem. Phys.*, **10**, 2053–2061, <https://doi.org/10.5194/acp-10-2053-2010>.
- , and —, 2011: Potential climatic impacts and reliability of large-scale offshore wind farms. *Environ. Res. Lett.*, **6**, 025101, <https://doi.org/10.1088/1748-9326/6/2/025101>.
- Wilczak, J., and Coauthors, 2015: The Wind Forecast Improvement Project (WFIP): A public–private partnership addressing wind energy forecast needs. *Bull. Amer. Meteor. Soc.*, **96**, 1699–1718, <https://doi.org/10.1175/BAMS-D-14-00107.1>.
- Wu, Y. T., and F. Porté-Agel, 2011: Large-eddy simulation of wind-turbine wakes: Evaluation of turbine parametrisations. *Bound.-Layer Meteorol.*, **138**, 345–366, <https://doi.org/10.1007/s10546-010-9569-x>.
- , and —, 2013: Simulation of turbulent flow inside and above wind farms: Model validation and layout effects.

- Bound.-Layer Meteor.*, **146**, 181–205, <https://doi.org/10.1007/s10546-012-9757-y>.
- Xia, G., and L. Zhou, 2017: Detecting wind farm impacts on local vegetation growth in Texas and Illinois using MODIS vegetation greenness measurements. *Remote Sens.*, **9**, 698, <https://doi.org/10.3390/rs9070698>.
- , —, J. M. Freedman, S. Baidya Roy, R. A. Harris, and M. C. Cervarich, 2016: A case study of effects of atmospheric boundary layer turbulence, wind speed, and stability on wind farm induced temperature changes using observations from a field campaign. *Climate Dyn.*, **46**, 2179–2196, <https://doi.org/10.1007/s00382-015-2696-9>.
- Yang, Z. L., and Coauthors, 2011: The community Noah land surface model with multiparameterization options (Noah-MP): 2. Evaluation over global river basins. *J. Geophys. Res.*, **116**, D12110, <https://doi.org/10.1029/2010JD015140>.
- Zhou, L., Y. Tian, S. Baidya Roy, C. Thorncroft, L. F. Bosart, and Y. Hu, 2012: Impacts of wind farms on land surface temperature. *Nat. Climate Change*, **2**, 539–543, <https://doi.org/10.1038/nclimate1505>.
- , —, —, Y. Dai, and H. Chen, 2013a: Diurnal and seasonal variations of wind farm impacts on land surface temperature over western Texas. *Climate Dyn.*, **41**, 307–326, <https://doi.org/10.1007/s00382-012-1485-y>.
- , —, H. Chen, Y. Dai, and R. A. Harris, 2013b: Effects of topography on assessing wind farm impacts using MODIS data. *Earth Interact.*, **17**, <https://doi.org/10.1175/2012E1000510.1>.